2020

Photoproduction of η Mesons Off the Proton For $1.2 < E_\gamma < 4.7$ GeV Using CLAS at Jefferson Laboratory

K. P. Adhikari
Old Dominion University, adhikari@jlab.org

M. J. Amaryan
Old Dominion University, mamaryan@odu.edu

G. Gavalian
Old Dominion University

M. Hattawy
Old Dominion University, mhattawy@odu.edu

M. Khachatryan
Old Dominion University, mkhachat@odu.edu

See next page for additional authors

Original Publication Citation

Hu, T., Akbar, Z., Crede, V., Adhikari, K., Adhikari, S., Amaryan, M., CLAS Collaboration (2020). Photoproduction of η mesons off the proton for $1.2 < E_\gamma < 4.7$ GeV using CLAS at Jefferson Laboratory. *Physical Review C, 102*(6), Article 065203. https://doi.org/10.1103/PhysRevC.102.065203

Photoproduction of η mesons off the proton for $1.2 < E_\gamma < 4.7$ GeV using CLAS at Jefferson Laboratory

T. Hu,[15] Z. Akbar,[15,*] V. Crede,[15,†] K. P. Adhikari,[35,‡] S. Adhikari,[14] M. J. Amaryan,[35] G. Angelini,[16] G. Asryan,[51] H. Atac,[41] C. Ayerbe Gayoso,[50] L. Barion,[18] M. Battaglieri,[42,20] I. Bedlinskiy,[31] F. Benmokhtar,[11] A. Bianconi,[45,23] A. S. Biselli,[12] F. Bossù,[7] S. Boiarinov,[42] W. J. Briscoe,[16] W. K. Brooks,[43] D. S. Carman,[42] J. Carvajal,[14] A. Celentano,[20] P. Chatagnon,[24] T. Chetry,[30] G. Ciullo,[18,13] L. Clark,[46] B. A. Clary,[9] P. L. Cole,[28,17] M. Contalbrigo,[18] R. Cruz-Torres,[29] A. D'Angelo,[21,38] N. Dashyan,[51] R. De Vita,[20] M. Defurne,[7] A. Deur,[42] S. Diehl,[9] C. Djalali,[34,40] M. Dugger,[2] R. Dupre,[24] H. Egiyan,[42] M. Ehrhart,[1] A. El Alaoui,[43] L. El Fassi,[30,1] P. Eugenio,[15] G. Fedotov,[39,§] R. Fersch,[8] A. Filippi,[22] G. Gavalian,[42,35] G. P. Gilfoyle,[37] F. X. Girod,[42,7] D. I. Glazier,[46] E. Golovatch,[39] R. W. Gothe,[40] K. A. Griffioen,[50] M. Guidal,[24] L. Guo,[14,42] K. Hafidi,[1] H. Hakobyan,[43,51] C. Hanretty,[42] N. Harrison,[42] M. Hattawy,[35] T. B. Hayward,[50] D. Heddle,[8,42] K. Hicks,[34] A. Hobart,[24] M. Holtrop,[32] Y. Ilieva,[40] I. Illari,[16] D. G. Ireland,[46] B. S. Ishkhanov,[39] E. L. Isupov,[39] D. Jenkins,[48] H. S. Jo,[27] K. Joo,[9] S. Joosten,[1,41] D. Keller,[49,34] M. Khachatryan,[35] A. Khanal,[14] M. Khandaker,[33,‖] A. Kim,[9] C. W. Kim,[16] W. Kim,[27] F. J. Klein,[6] V. Kubarovsky,[42] L. Lanza,[21] M. Leali,[45,23] P. Lenisa,[13,18] K. Livingston,[46] I. J. D. MacGregor,[46] D. Marchand,[24] N. Markov,[9] V. Mascagna,[44,23,¶] M. E. McCracken,[5] B. McKinnon,[46] C. A. Meyer,[5] Z. E. Meziani,[1,41] T. Mineeva,[43] V. Mokeev,[42] A. Movsisyan,[18] E. Munevar,[16,#] C. Munoz Camacho,[24] P. Nadel-Turonski,[42,6] S. Niccolai,[24] G. Niculescu,[26] T. O'Connell,[9] M. Osipenko,[20] A. I. Ostrovidov,[15] M. Paolone,[41] L. L. Pappalardo,[13,18] R. Paremuzyan,[32] E. Pasyuk,[42] W. Phelps,[8] O. Pogorelko,[31] J. Poudel,[35] J. W. Price,[3] Y. Prok,[35] D. Protopopescu,[46] B. A. Raue,[14,42] M. Ripani,[20] J. Ritman,[25] A. Rizzo,[21,38] G. Rosner,[46] J. Rowley,[34] F. Sabatié,[7] C. Salgado,[33] A. Schmidt,[29,**] R. A. Schumacher,[5] Y. G. Sharabian,[42] U. Shrestha,[34] Iu. Skorodumina,[40,39] D. Sokhan,[46] O. Soto,[19] N. Sparveris,[41] S. Stepanyan,[42] P. Stoler,[36] I. I. Strakovsky,[16] S. Strauch,[40] J. A. Tan,[27] N. Tyler,[40] M. Ungaro,[42,9] L. Venturelli,[45,23] H. Voskanyan,[51] E. Voutier,[24] D. P. Watts,[47] K. Wei,[9] X. Wei,[42] M. H. Wood,[4] N. Zachariou,[47] J. Zhang,[49,35] and Z. W. Zhao[10,35]

(CLAS Collaboration)

[1]*Argonne National Laboratory, Argonne, Illinois 60439, USA*
[2]*Arizona State University, Tempe, Arizona 85287-1504, USA*
[3]*California State University, Dominguez Hills, Carson, California 90747, USA*
[4]*Canisius College, Buffalo, New York 14208, USA*
[5]*Carnegie Mellon University, Pittsburgh, Pennsylvania 15213, USA*
[6]*Catholic University of America, Washington, DC 20064, USA*
[7]*IRFU, CEA, Université Paris-Saclay, F-91191 Gif-sur-Yvette, France*
[8]*Christopher Newport University, Newport News, Virginia 23606, USA*
[9]*University of Connecticut, Storrs, Connecticut 06269, USA*
[10]*Duke University, Durham, North Carolina 27708-0305, USA*
[11]*Duquesne University, Pittsburgh, Pennsylvania 15282, USA*
[12]*Fairfield University, Fairfield, Connecticut 06824, USA*
[13]*Università di Ferrara, 44121 Ferrara, Italy*
[14]*Florida International University, Miami, Florida 33199, USA*
[15]*Florida State University, Tallahassee, Florida 32306, USA*
[16]*The George Washington University, Washington, DC 20052, USA*
[17]*Idaho State University, Pocatello, Idaho 83209, USA*
[18]*INFN, Sezione di Ferrara, 44100 Ferrara, Italy*
[19]*INFN, Laboratori Nazionali di Frascati, 00044 Frascati, Italy*

[*]Present address: University of Virginia, Charlottesville, Virginia 22901, USA.
[†]crede@fsu.edu
[‡]Present address: Mississippi State University, Mississippi State, Mississippi 39762-5167, USA.
[§]Present address: Ohio University, Athens, Ohio 45701, USA.
[‖]Present address: Idaho State University, Pocatello, Idaho 83209, USA.
[¶]Present address: Università degli Studi di Brescia, 25123 Brescia, Italy.
[#]Present address: Thomas Jefferson National Accelerator Facility, Newport News, Virginia 23606, USA.
[**]Present address: The George Washington University, Washington, DC 20052, USA.

[20]*INFN, Sezione di Genova, 16146 Genova, Italy*
[21]*INFN, Sezione di Roma Tor Vergata, 00133 Rome, Italy*
[22]*INFN, Sezione di Torino, 10125 Torino, Italy*
[23]*INFN, Sezione di Pavia, 27100 Pavia, Italy*
[24]*Université Paris-Saclay, CNRS/IN2P3, IJCLab, 91405 Orsay, France*
[25]*Institute für Kernphysik, 52425 Jülich, Germany*
[26]*James Madison University, Harrisonburg, Virginia 22807, USA*
[27]*Kyungpook National University, Daegu 41566, Republic of Korea*
[28]*Lamar University, 4400 MLK Blvd, P.O. Box 10009, Beaumont, Texas 77710, USA*
[29]*Massachusetts Institute of Technology, Cambridge, Massachusetts 02139-4307, USA*
[30]*Mississippi State University, Mississippi State, Mississippi 39762-5167, USA*
[31]*National Research Centre Kurchatov Institute-ITEP, Moscow, 117259, Russia*
[32]*University of New Hampshire, Durham, New Hampshire 03824-3568, USA*
[33]*Norfolk State University, Norfolk, Virginia 23504, USA*
[34]*Ohio University, Athens, Ohio 45701, USA*
[35]*Old Dominion University, Norfolk, Virginia 23529, USA*
[36]*Rensselaer Polytechnic Institute, Troy, New York 12180-3590, USA*
[37]*University of Richmond, Richmond, Virginia 23173, USA*
[38]*Università di Roma Tor Vergata, 00133 Rome, Italy*
[39]*Skobeltsyn Institute of Nuclear Physics, Lomonosov Moscow State University, 119234 Moscow, Russia*
[40]*University of South Carolina, Columbia, South Carolina 29208, USA*
[41]*Temple University, Philadelphia, Pennsylvania 19122, USA*
[42]*Thomas Jefferson National Accelerator Facility, Newport News, Virginia 23606, USA*
[43]*Universidad Técnica Federico Santa María, Casilla 110-V Valparaíso, Chile*
[44]*Università degli Studi dell'Insubria, 22100 Como, Italy*
[45]*Università degli Studi di Brescia, 25123 Brescia, Italy*
[46]*University of Glasgow, Glasgow G12 8QQ, United Kingdom*
[47]*University of York, York YO10 5DD, United Kingdom*
[48]*Virginia Tech, Blacksburg, Virginia 24061-0435, USA*
[49]*University of Virginia, Charlottesville, Virginia 22901, USA*
[50]*College of William and Mary, Williamsburg, Virginia 23187-8795, USA*
[51]*Yerevan Physics Institute, 375036 Yerevan, Armenia*

(Received 15 June 2020; revised 5 October 2020; accepted 24 November 2020; published 14 December 2020)

Photoproduction cross sections are reported for the reaction $\gamma p \to p\eta$ using energy-tagged photons and the CLAS spectrometer at Jefferson Laboratory. The η mesons are detected in their dominant charged decay mode, $\eta \to \pi^+\pi^-\pi^0$, and results on differential cross sections are presented for incident photon energies between 1.2 and 4.7 GeV. These new η photoproduction data are consistent with earlier CLAS results but extend the energy range beyond the nucleon resonance region into the Regge regime. The normalized angular distributions are also compared with the experimental results from several other experiments, and with predictions of η-MAID 2018 and the latest solution of the Bonn-Gatchina coupled-channel analysis. Differential cross sections $d\sigma/dt$ are presented for incident photon energies $E_\gamma > 2.9$ GeV ($W > 2.5$ GeV), and compared with predictions which are based on Regge trajectories exchange in the t-channel (Regge models). The data confirm the expected dominance of ρ, ω vector-meson exchange in an analysis by the Joint Physics Analysis Center.

DOI: 10.1103/PhysRevC.102.065203

I. INTRODUCTION

The photoproduction of pseudoscalar mesons on the nucleon has remained of interest in recent years for the study of meson production in hadronic reactions across a wide range of energies. At low energies using incident photon energies below 3.0 GeV, information about the nucleon excitation spectrum can be extracted, whereas at higher energies above $E_\gamma \approx 4$ GeV, details of the residual hadron interactions due to the t-channel exchange of massive quasi-particles known as Reggeons can be studied [1]. These two regimes are analytically connected, but the scarcity of cross section and polarization data for the energy range 3–6 GeV have thus far hindered our understanding of the transition from the baryon resonance regime to high-energy photoproduction. While each Reggeon exchange has a known energy behavior, the dependence on the momentum exchange in the reaction is initially unknown. However, dispersion relations can be used to derive the t-dependence of the Regge amplitudes from the low-energy amplitude, which is usually described in terms

of a finite number of partial waves. This technique of finite-energy sum rules (FESR) was recently applied to π^0 and η photoproduction [2,3]. In these reactions, the resonance and the Regge regions can be effectively separated. Low-energy amplitudes, which directly contain the resonance dynamics, should then smoothly connect with the high-energy region [4]. Alternatively, FESR can be derived to constrain the low-energy amplitudes by the t-channel Reggeon exchanges [5] and ultimately, to extract nucleon resonance parameters. Both approaches were recently explored for π^0 photoproduction in Ref. [6].

In the nucleon resonance region, abundant data on η photoproduction on the proton are available from the reaction threshold at $W_{\text{thres.}} \approx 1.49\,\text{GeV}$ up to the fourth resonance region just below $W \approx 2\,\text{GeV}$. The data situation has even improved in recent years, particularly for (double-)polarization observables with the availability of longitudinally and transversely polarized targets at several photoproduction facilities around the world, e.g., Jefferson Laboratory [7] in Newport News, USA, ELSA [8] in Bonn, Germany, and MAMI [9] in Mainz, Germany. Data using high-intensity photon beams with excellent linear polarization are also available from the GRAAL facility [10] in Grenoble, France, and from LEPS [11] at SPring-8 in Hyogo, Japan. The photo-induced production of η mesons is a selective probe for the study of nucleon excitations. Although photons incident on protons couple to both isospin $I = 0, 1$ initial states, the η meson in the final state serves as an isospin filter for baryon excitations since isospin $I = 3/2$ states (Δ resonances) are prohibited from decaying into $N\eta$ final states.

Near the production threshold, the dominance of the two nucleon resonances $N(1535)\,1/2^-$ and $N(1650)\,1/2^-$ in η photoproduction is undisputed [12,13]. Small contributions have also been observed in (γ, η) from the $N(1520)\,3/2^-$ state, which itself couples strongly to the $N\eta$ decay mode. The state was identified mainly from the S_{11}-D_{13} interference term in the description of the photon-beam asymmetry [14–17] indicating the importance of polarization observables. Also available are results from MAMI for the transverse target asymmetry T, and the beam-target asymmetry F [18]. The helicity asymmetry E was reported by the CLAS Collaboration at Jefferson Lab [19] and the A2 Collaboration at MAMI [20]. More recently, results on the target asymmetry T and the double-polarization observables E, G (longitudinal target polarization) as well as P, H (transverse target polarization) in the photoproduction of η mesons off protons were reported by the CBELSA/TAPS Collaboration at ELSA [21].

In their biannual editions, the listing of nucleon resonances by the Particle Data Group (PDG) in the *Review of Particle Physics* [22] has undergone significant upgrades based on the recent photoproduction data from the above facilities with almost no N^* resonance left untouched since 2010. Several new nucleon states have been added, some of which show strong couplings to $N\eta$. Above 1700 MeV in overall center-of-mass energy, a third $1/2^-$ state, $N(1895)\,1/2^-$, is now listed as a new resonance with a four-star rating indicating its existence is certain in both its overall status and its $N\eta$ decay mode. In the $1/2^+$ wave, a large contribution in (γ, η) is observed from the $N(1710)\,1/2^+$ resonance, the status of which has been upgraded to three stars in its $N\eta$ decay mode. In the fourth resonance region and above, discrepancies occur in various amplitude analyses. Such ambiguities are not surprising in light of the remaining *incompleteness* of the η photoproduction database. The experimental status of η photoproduction from nucleons and nuclei, as well as phenomenological progress was recently reviewed in Ref. [23].

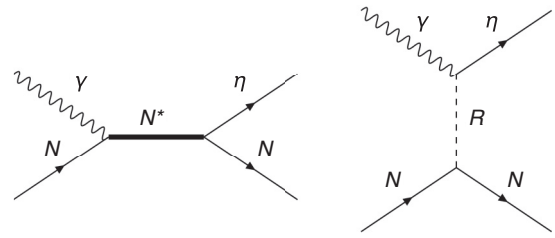

FIG. 1. Dominant contributions to η photoproduction off the nucleon: s-channel intermediate nucleon resonance excitation (left) and t-channel exchange of Reggeons (right).

The theoretical description of high-energy photoproduction provides constraints on the amplitudes utilized in low-energy meson photoproduction to extract the spectrum of excited baryons [6]. Moreover, understanding the meson photoproduction mechanism at high energies is a crucial component of a broader program to search for gluonic excitations in the meson spectrum, which is the primary goal of the GlueX experiment in Hall D at Jefferson Lab [24,25].

In a brief summary, η photoproduction off the nucleon is dominantly described by s-channel intermediate nucleon resonance excitation (left side of Fig. 1) close to the production threshold with an admixture of t-channel exchange of Reggeons (right side of Fig. 1) as the incident photon energy increases, whereas the t-channel Reggeon exchange dominates the production of η mesons at higher energies above 7 GeV.

In this paper, differential cross sections are presented for the reaction $\gamma p \to p\eta$ from CLAS at Jefferson Lab, where the η was identified through the detection of its decay products $\pi^+\pi^-\pi^0$. The new data reported here cover an incident photon energy range E_γ from 1.2 GeV up to 4.7 GeV.

This paper has the following structure. A summary of previous measurements in η photoproduction is presented in Sec. II. Section III gives an introduction to the CLAS-g12 experimental setup. The data reconstruction and event selection are discussed in Sec. IV and the extraction of the cross sections is described in Sec. V. Finally, the experimental results and a discussion of the physics including possible nucleon resonance contributions are presented in Secs. VI and VII, respectively.

II. PREVIOUS MEASUREMENTS

Cross sections for the reaction $\gamma p \to p\eta$ were measured at many different laboratories over a wide kinematic range and in various η decay modes using either tagged-photon beams produced in Compton scattering of laser photons off electrons in the accelerator [16,26,27] or via the bremsstrahlung technique [28–33]. A summary of the experimental data on

TABLE I. Summary of experimental data on cross sections for η photoproduction off the nucleon.

Reaction	W [GeV]	$-t$ [GeV^2]	Reference
$\gamma p \to p\eta$	1.49 – 1.96	–	A2 [32,33]
	1.55 – 2.80	–	CLAS [30,48]
	1.51 – 2.55	–	CB-ELSA [28,29]
	1.57 – 2.38	–	CBELSA/TAPS [31]
	1.49 – 1.92	–	GRAAL [16,26]
	1.97 – 2.32	–	LEPS [27]
	2.36 & 2.55	0.2–1.2	Daresbury [35]
	2.90 & 3.48	0.0–1.4	DESY [36]
	2.90	<1.0	MIT [38]
	3.48–5.56	0.2–0.9	SLAC [40]
	2.90–3.99	0.3–0.8	Cornell [39]
$\gamma n \to n\eta$	1.49–1.88	–	A2 [45]
	1.50–2.18	–	CBELSA/TAPS [46]
	1.59–2.07	–	CBELSA/TAPS [47]

η photoproduction cross sections from the nucleon is given in Table I. The current status of single-η meson production using photon beams is reviewed in Ref. [34], and in particular the information that can be obtained on the spectrum of light, nonstrange baryons.

A whole "industry" of photoproduction experiments recorded data for several meson-production channels in the 1960s and '70s. Results were mostly published at higher energies and only a few data points bridge the gap down to the resonance region below $E_\gamma \approx 3$ GeV. Particularly interesting for the discussion of cross sections is the normalization technique of these older data since tagged-photon beams were not available at these facilities.

A. Summary of older photoproduction experiments (1960s and 1970s)

At the 5 GeV electron synchrotron NINA at the Daresbury Laboratory, a linearly polarized bremsstrahlung beam was used to extract differential cross sections for the reaction $\gamma p \to p\eta$ at incident photon energies of 2.5 and 3.0 GeV, and for various t-values between -0.2 and -1.2 GeV^2 [35]. The incident photon intensity as a function of energy was derived from a quantameter, together with the shape of the spectrum as measured with a pair spectrometer. At the Deutsches Elektronen-Synchrotron (DESY), a bremsstrahlung beam was produced on a tungsten target and the flux was measured with a gas-filled quantameter. Cross section results for η photoproduction were reported at mean photon energies of 4 and 6 GeV in the momentum transfer range between zero and 1.4 GeV^2 [36].

A bremsstrahlung beam from a tungsten target was used at the Cambridge Electron Accelerator (CEA) at the Massachusetts Institute of Technology (MIT). The beam was monitored with a quantameter that was calibrated against a Faraday cup and whose output was measured with a current integrator [37]. Results for η photoproduction at 4 GeV were published in Ref. [38]. Finally, cross section measurements were also performed at the 10 GeV synchrotron at the Laboratory of Nuclear Studies at Cornell University. Several data points were published for incident photon energies of 4 and 8 GeV and momentum tranfers $-t$ between 0.3 and 0.8 GeV^2 [39].

Measurements at higher incident photon energies in the range 6.0–16.0 GeV were performed at the Stanford Linear Accelerator Center (SLAC) using a bremsstrahlung beam [40]. The beam was monitored by detecting Cherenkov light of e^+e^- pairs from a converter in the beam. The Cherenkov monitor was calibrated against a precision calorimeter [41]. In Ref. [42], the overall uncertainty in normalization was estimated at 10 %; other references give even smaller uncertainties, see e.g. Ref. [41]. The SLAC high-power quantameter was used for the measurement of the incident photon flux and is described in Ref. [43].

B. Experiments using Compton backscattering

The GRenoble Anneau Accelerateur Laser (GRAAL) experiment measured the differential η photoproduction cross sections from threshold up to 1100 MeV [26] and up to 1500 MeV [16] in incident photon laboratory energy and for $\cos\theta_{\text{c.m.}} < 0.85$ of the η meson in the overall center-of-mass (c.m.) frame. The facility was located at the European Synchrotron Radiation Facility (ESRF) in Grenoble, France. For a detailed description of the facility, see Ref. [10]. The tagged and polarized γ-ray beam was produced by Compton scattering of laser photons off the 6 GeV electrons circulating in the storage ring. The photon energy was provided by an internal tagging system consisting of silicon microstrips for the detection of the scattered electron and a set of plastic scintillators for time-of-flight (TOF) measurements [16]. A thin monitor was used to measure the beam flux (typically 10^6 γ/s). The monitor efficiency of $(2.68 \pm 0.03)\%$ was estimated by comparing with the response of a lead/scintillating fiber calorimeter at a low rate.

At the SPring-8/LEPS facility, the photon beam was produced by backward-Compton scattering of laser photons off electrons with an energy of 8 GeV. Data were accumulated with 1.0×10^{12} photons at the target and cross section results on the reaction $\gamma p \to p\eta$ were extracted for the incident photon energy range $E_\gamma \in [1.6, 2.4]$ GeV in the backward direction ($\cos\theta_{\text{c.m.}} < -0.6$) [27].

C. Experiments using bremsstrahlung photons

At the ELectron Stretcher Accelerator (ELSA) [8], two very different experimental setups extracted cross section data for the photo-produced $p\eta$ final state. In 2001, the CB-ELSA detector recorded data and η photoproduction was studied in the neutral decays of the η meson into $\gamma\gamma$ and $\pi^0\pi^0\pi^0$ [28,29]. The original experiment consisted of the CsI(Tl)-based Crystal Barrel (CB) calorimeter covering 97.8 % of the 4π solid angle [44]. For the 2000/2001 data taking, electrons were extracted in two separate experiments at energies of 1.4 and 3.2 GeV, covering tagged-photon energies from 0.3 up to about 3.0 GeV, with a typical intensity of 1–3 $\times$ 10^6 tagged photons/s. The experimental setup was later modified and in a series of measurements in 2002/2003, a combination

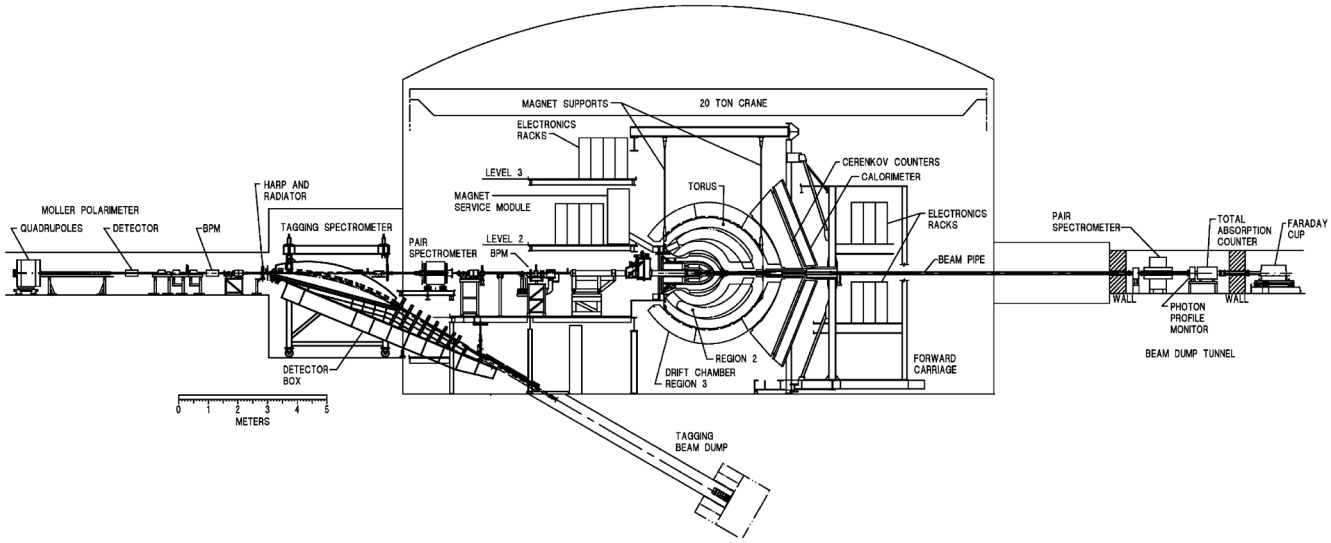

FIG. 2. Side view of the CLAS detector in Hall B at Jefferson Lab including the photon tagging facility upstream of CLAS. Reproduced figure with permission from Ref. [7]. Copyright 2003 by Elsevier.

of the CB calorimeter and the BaF_2 TAPS detector in the forward direction was used. Results of the CBELSA/TAPS setup on single-η cross section measurements off the proton can be found in Ref. [31]. The data provide improved angular coverage in the forward and backward direction in the center-of-mass system.

At the upgraded Mainz Microtron (MAMI-C), an experimental setup using a combination of the NaI(Tl) Crystal Ball and BaF_2 TAPS multiphoton spectrometers recorded high-quality data on the reaction $\gamma p \to p\eta$ in the energy range from the production threshold at 707 MeV to 1.4 GeV [32,33]. The NaI(Tl) crystals were arranged in two hemispheres that covered 93 % of the 4π solid angle and the TAPS calorimeter subtended the full azimuthal range for polar angles from 1° to 20°. Since the TAPS calorimeter was installed 1.5 m downstream of the Crystal Ball center, the resolution of TAPS in the polar angle θ was better than 1°. For an electron beam energy of 1508 MeV, a tagger channel in this experiment had a width of about 2 MeV at $E_\gamma = 1402$ MeV and about 4 MeV at the η-photoproduction threshold of $E_\gamma = 707$ MeV.

At the Continuous Electron Beam Accelerator Facility (CEBAF) at Jefferson Laboratory (Jefferson Lab), the CEBAF Large Acceptance Spectrometer (CLAS) was optimized for charged-particle tracking. A detailed description of the spectrometer and its various detector components is given below and in Ref. [7]. The CLAS "g1" experiment accumulated data in 1998 (g1a) and in 1999 (g1c) using electron beam energies of 2.49 and 2.45 GeV, respectively. These experiments used a single-prong trigger configuration. Results for the reaction $\gamma p \to p\eta$ were only published from the CLAS "g1a" experiment [48]. For the absolute normalization of the η channel, the SAID-SM02 solution [49] was used. The normalization uncertainty for all incident photon energies below 2 GeV was estimated at 3% [48].

The CLAS "g11a" experiment accumulated a high-statistics data sample in 2004 of about 20×10^9 triggered events. An electron beam of energy $E_{e^-} = 4.023$ GeV was used to generate tagged photons with energies between 0.81 and 3.81 GeV covering center-of-mass energies up to $\sqrt{s} \approx 2.84$ GeV. Results on η cross section measurements for $E_\gamma < 3.5$ GeV are published in Ref. [30].

A review of the main photoproduction data sets prior to 2013 and a corresponding comparison of their coverage in energy and solid angle can be found in Ref. [50].

III. EXPERIMENTAL SETUP

The $\gamma p \to p\eta$ measurements discussed here were performed at Jefferson Lab from March to June 2008 using the CLAS spectrometer [7] in Hall B. The experimental setup is shown in Fig. 2. The incident tagged, bremsstrahlung photon beam was produced from a 60–65 nA electron beam of energy $E_{e^-} = 5.715$ GeV delivered by the CEBAF accelerator. These measurements were part of the CLAS-g12 experiment, which was a high-luminosity data-taking period. The tagging system provided a circularly polarized, real-photon beam with the highest available photon energies of any CLAS experiment of up to $E_\gamma \approx 5.4$ GeV, corresponding to about 95% of E_{e^-}. The photons impinged upon a 40-cm-long unpolarized liquid-hydrogen target, which was moved upstream by 90 cm from the center of the CLAS spectrometer to enhance the acceptance of charged tracks in the forward direction. Various results from the CLAS-g12 experiment have been recently published and are discussed in Refs. [51–54]. First cross section measurements have been presented in short papers on the reaction $\gamma p \to p\pi^0 \to pe^+e^-(\gamma)$ [52] and on the reaction $\gamma p \to K^+K^+(X)$ [54] in the search for excited Ξ baryons.

A brief overview of the CLAS performance is given in the following section; a full description of the CLAS spectrometer can be found in Ref. [7]. The remaining sections describe at greater length those components of the experimental setup that differ from previous CLAS experiments or are particularly relevant for the cross section measurements.

A. Overview

The charged tracks in the experiment were detected in the CLAS spectrometer, which provided coverage for charged particles in the polar-angle range $8^\circ < \theta_{\rm lab} < 135^\circ$. The three momentum components of the particles were reconstructed from their tracks in the toroidal magnetic field of the spectrometer by a set of three drift-chamber packages [55]. Time-of-flight (TOF) information was available from plastic scintillators [56] located about 5 m from the center of CLAS. The spectrometer provided a momentum and angle resolution of $\Delta p/p \approx 1\%$ and $\Delta\theta \approx 1^\circ$–$2^\circ$, respectively. A set of plastic scintillation counters close to the target (referred to as the start counter) provided event start times [57]. For this experiment, coincident signals from the photon tagger, start counter, and time-of-flight system constituted the event trigger that required a coincidence between a scattered-electron signal from the photon tagger and an energy-dependent number of charged tracks in CLAS (see Sec. III E for details).

B. The tagging system

The bremsstrahlung beam was produced from a thin gold radiator and photons were tagged by detecting energy-degraded electrons, which were deflected in the magnetic field of a single dipole magnet. The CLAS tagging system used a hodoscope that contained two planar arrays of plastic scintillators [58]. The first layer of 384 partially overlapping small scintillators (E-counters) provided the photon energy accuracy of $\approx 1 \times 10^{-3}\, E_{e^-}$, while the second layer of 61 larger scintillators (T-counters) provided the timing resolution of about 160 ps necessary to form a coincidence with the corresponding charged particles that were produced in the nuclear interaction triggered by the tagged photon.

The arrangement of the E-counters is relevant for the discussion of the cross-section results presented here. The widths of the counters ranged from 6 to 18 mm to provide approximately constant momentum intervals of $0.003\, E_{e^-}$. Since each counter optically overlapped its adjacent neighbors by one-third of their respective widths, a total of 767 separate incident photon energy bins was available with an energy range of approximately $r = 0.001\, E_{e^-}$. Assuming equal acceptance along the length of each paddle, the element for the photon energy in the covariance matrix is given by

$$\sigma^2_{E_\gamma} = \frac{1}{r}\int_{-r/2}^{r/2} E^2\, dE = \frac{r^2}{12}. \tag{1}$$

The CLAS-g12 experiment recorded data at the highest possible CEBAF energies of $E_{e^-} = 5.715$ GeV and therefore, $\sigma_{E_\gamma} = 1.65$ MeV, which is about 80% greater than the number for the CLAS-g11a experiment [30]. Thus, a slightly broader binning in center-of-mass energy W was chosen for $W < 2.1$ GeV. In particular, very close to the low-energy end of the tagging range at about 21% of E_{e^-}, the width of the W bins translates into the smallest bin width in incident photon energy for the entire analyzed energy range. This resolution effect, combined with observed small fluctuations in our extracted cross sections at the lower end of the tagging range, which are believed to originate from the measured incident photon flux, required adjusting the W binning from 20 to 40 MeV for $W < 1.88$ GeV.

C. Particle identification

Particle identification (PID) of charged final-state hadrons in this experiment was based on the combined information from the drift chamber and TOF systems. A value for β, defined as the ratio of the particle speed relative to the speed of light, could be measured in two different ways:

(1) An empirically measured value for each particle, $\beta_m = v/c = \Delta t/(c\, l)$, was based on timing information from the time-of-flight and start counter systems (where l denotes the length of the track as determined from the drift-chamber track reconstruction), and
(2) Independently, a value for each particle, $\beta_c = p/E$, could be determined from the measured momentum using the CLAS drift chambers and the PDG mass [22] for the particle.

PID could then proceed by evaluating the distribution of $\Delta\beta = |\beta_c - \beta_m|$ values and defining proper event-by-event selection criteria.

The CEBAF electrons were delivered to the CLAS-g12 experiment in 2-ns bunches. Several bunches arrived at the tagger within the trigger coincidence window and each bunch contained many electrons. Therefore, many photon candidates were recorded for each event; random hits could also occur from background sources, e.g., cosmic radiation. To determine the correct initial-state photon, which triggered the hadronic reaction at the event vertex in the liquid-hydrogen target, the time differences were used between the event vertex-time based on the final-state tracks and the tagger vertex-time for each photon candidate.

The event vertex-time, $t_{\rm event}$, was given as an average over the event's track times,

$$t_{\rm track} = t_{\rm ST} - \frac{d}{c\,\beta_m}, \tag{2}$$

where $t_{\rm ST}$ denotes the start-counter time and d is the distance from the interaction point to the corresponding start-counter paddle. The time, t_γ, for each photon candidate is given by the recorded electron-triggered tagger time corrected for the propagation from the center of the liquid-hydrogen target to the event vertex along the beam axis. Figure 3 shows the coincidence time $\Delta t_{\rm TGPB} = t_{\rm event} - t_\gamma$. The 2-ns time structure is clearly visible. In the CLAS-g12 experiment, selecting photons from the central coincidence peak and discarding events with more than one photon candidate resulted in a remaining nonnegligible accidental background of about 13% due to the relatively high electron beam current of 60–65 nA.

D. The liquid-hydrogen target

In the CLAS-g12 experiment, the liquid-hydrogen target was not positioned at the center of CLAS but was moved upstream by 90 cm to allow for the enhanced detection of peripherally produced mesons off the proton with the goal to search for and study excited mesons at the highest available CEBAF energies. Peripheral reactions are characterized

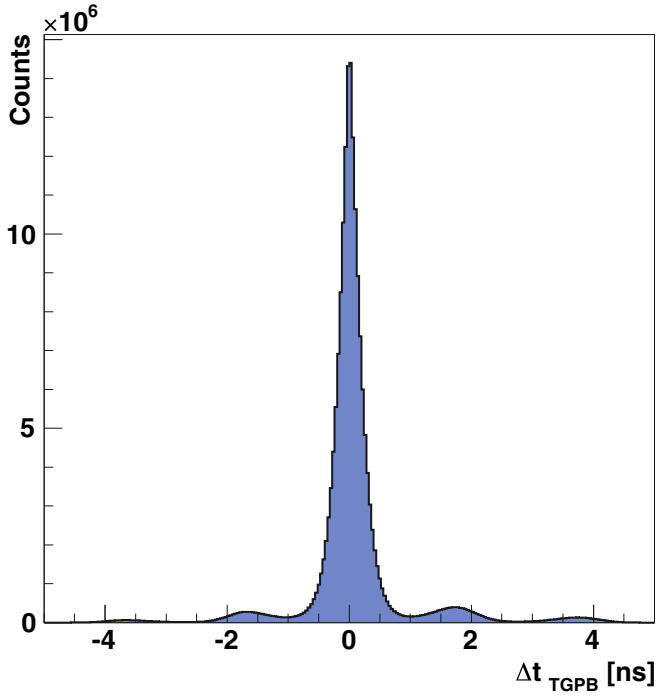

FIG. 3. Distribution of the tagger-start counter coincidence times. The 2-ns bunch structure is visible. Events were considered for further analysis only if a single photon candidate remained after a timing cut of $|\Delta t_{\mathrm{TGPB}}| < 1$ ns.

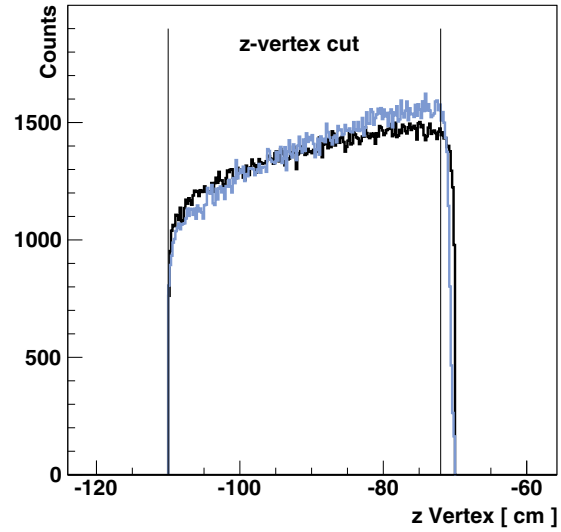

FIG. 4. The z-vertex distribution of $\gamma p \to p\eta$ Monte Carlo (black) and data events (blue). The target length of 40 cm is clearly visible. In this experiment, the target cell was moved upstream from the CLAS center by 90 cm. The vertical lines define the range of the z-vertex cut.

by small values of the exchanged four-momentum $-t$ and are strongly forward peaked at high energies since the cross section is almost exponentially falling with t. The target cell was 40 cm in length and 2 cm in diameter. The z-vertex distributions (coordinate along the beamline) for data and Monte Carlo events are shown in Fig. 4. The target length and the position offset from the CLAS center are clearly visible.

In the CLAS-g12 experiment, the target temperature and pressure were sampled continuously throughout each run. Since the overall uncertainty in the target density was smaller than the geometrical uncertainty in the dimensions of the Kapton cell, the uncertainty in the liquid-hydrogen density was not considered a factor in the budget of the various systematic uncertainties.

E. Trigger

The entire CLAS-g12 data set was classified into many different groups of runs according to their trigger configurations. Some of these configurations applied a tagger *prescaling* to enhance events with high photon energies. For this analysis, we used a fraction of the total statistics that was not subject to prescaling to avoid additional complications in the absolute normalization of the measured angular distributions.

The TOF counters generated signals for the CLAS level-1 trigger. These detectors were positioned outside the CLAS tracking system in a symmetric six-sector arrangement, geometrically defined by the coils of the CLAS toroidal magnet. For the data presented here, the trigger required a scattered electron in the bremsstrahlung tagger in coincidence with either (a) (at least) three charged tracks in different sectors with no restrictions on any photon energy, or (b) only two tracks in different sectors with the additional requirement of observing at least one tagger photon with an energy above 3.6 GeV. Along with several ancillary trigger conditions, these requirements resulted in a live time of the data-acquisition system of about 87%. About 20–30 recorded photons per event were observed using a trigger coincidence window of approximately 100 ns.

IV. CALIBRATION AND EVENT RECONSTRUCTION

The calibration of the individual spectrometer components followed the CLAS standard procedures [59]. In the process, inefficient TOF paddles were identified and later removed from the analysis in a standardized approach for real data and simulated events. The latter is particularly important for the trigger simulation. The details of the Monte Carlo simulations are described in Sec. IV C.

Charged particles emerging from the event vertex interact with various detector components and materials, e.g., target, beam pipe, and start counter, and therefore, are subject to energy loss along their trajectories. A standard CLAS software package [60] was applied to account for these interactions. The CLAS drift chambers existed as three drift-chamber regions, which were located at three positions in the radial direction [55]. Therefore, each particle track also needed to be corrected for momentum owing to small misalignments of these three regions and fluctuations in the toroidal magnetic field. The momentum corrections for each charged particle were determined in kinematic fitting for the exclusive $\gamma p \to p\pi^+\pi^-$ reaction, where the mean values of the corresponding momentum pull distributions were tuned in an iterative procedure. The corrections were small and typically of the order of

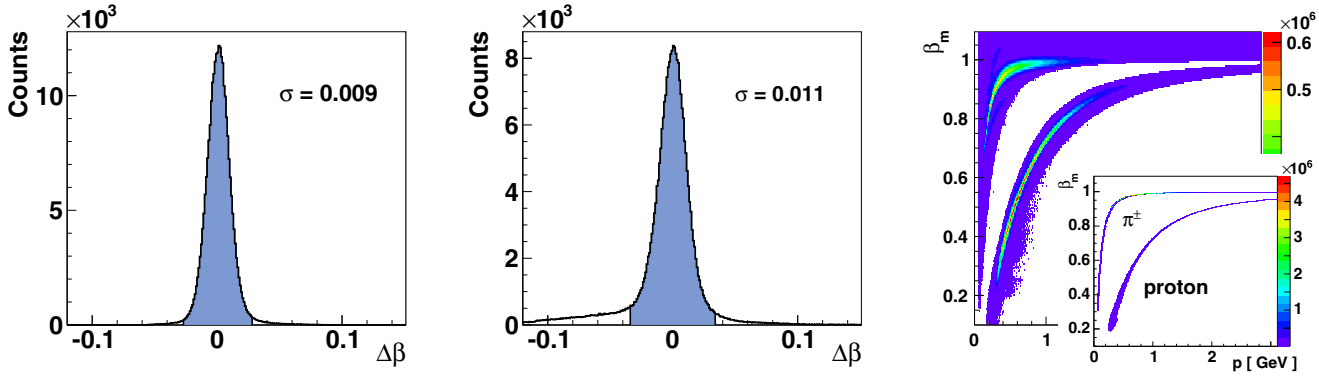

FIG. 5. Left and middle: $\Delta\beta = |\beta_c - \beta_m|$ distributions for protons and positively charged pions, respectively. The blue area indicates the 3σ cut according to Eq. (3). Right: The distribution of β_m vs. particle momentum before and after (inset) the 3σ cut. Note that the momentum range in the inset is limited to $p < 3.1$ GeV to better illustrate the separation of the two bands at low momenta.

a few MeV. The set of simulated events did not undergo any momentum corrections.

A. Preparation of the $\pi^+\pi^-\pi^0$ final state

The reconstruction of the $p\eta$ channel was based on preparing a data set of photoproduced $p\pi^+\pi^-\pi^0$ events. The same data set was also used to extract the cross sections for the reactions $\gamma p \to p\omega \to p(\pi^+\pi^-\pi^0)_\omega$ and $\gamma p \to K^0\Sigma^+ \to (\pi^+\pi^-)_{K^0}(p\pi^0)_{\Sigma^+}$, which will be discussed in subsequent publications. The only major difference in extracting the cross sections for these three reactions was the subtraction of background events. For this reason, this section will focus on the reconstruction of the general reaction $\gamma p \to p\pi^+\pi^-\pi^0$, followed by a separate section on describing the background subtraction. The preparation of the final $p\eta$ event sample resulted in the reconstruction of ≈293 000 $\eta \to \pi^+\pi^-\pi^0$ signal events for the incident photon energy range $1.18 < E_\gamma < 4.72$ GeV or $1.76 < W < 3.12$ GeV in center-of-mass energy. Note that 4.72 GeV corresponds to 82.6% of $E_{e^-} = 5.715$ GeV and is the highest incident-photon energy that just provides sufficient statistics for this analysis.

B. Event reconstruction and selection criteria

The CLAS spectrometer was optimized for detecting and measuring charged particles. However, the overconstrained event kinematics allows for the reconstruction of a single neutral meson. The reaction $\gamma p \to p\pi^+\pi^-(\pi^0)$ with a missing π^0 was identified in a first step by requiring exactly one proton track and two charged-pion tracks. Positively and negatively charged pions were distinguished by their track curvatures in the toroidal field. The acceptance of π^- mesons was smaller than for π^+ mesons since negatively charged tracks were bent toward the beamline and a large fraction escaped through the forward hole of the CLAS spectrometer. The π^0 meson was later identified in kinematic fitting.

Standard particle identification was then improved by evaluating $\Delta\beta$ distributions and applying a 3σ cut on either the proton or the π^+ meson:

$$\Delta\beta = |\beta_c - \beta_m| = \left| \sqrt{\frac{p^2}{m^2 + p^2}} - \beta_m \right| < 3\sigma, \quad (3)$$

where β_m and β_c are based on information from the TOF and the drift-chamber system, respectively, as defined in Sec. III C. While the quantity $\Delta\beta$ depends on particle momentum, the $\Delta\beta$ distribution is approximately Gaussian when summed over all β_m values, with width $\sigma = 0.009$ and 0.011 for the proton and pions, respectively. Figure 5 shows the $\Delta\beta$ distributions for protons (left) and charged pions (center). The tail on the left side of the $\Delta\beta$ peak for pions originates from misidentified electrons. This small lepton contamination is not a concern since these events did not pass the kinematic fitter, which is described below. Also shown in Fig. 5 (right) is the distribution of β_m versus particle momentum before and after (inset) the 3σ cut according to Eq. (3). Clear bands for the proton and the pions are visible.

Standard fiducial cuts [59] geometrically suppressed events outside of the active detector regions where the acceptance was well behaved and reliably reproduced in simulations. For example, the magnetic field varied rapidly close to the torus coils rendering these regions difficult to simulate. This effect was more dramatic in the forward direction, where the coils occupied a larger amount of the solid angle for small polar angles. Such regions were studied for charged hadrons with exclusive $\gamma p \to p\pi^+\pi^-$ events and defined as upper and lower limits of the azimuthal angle $\phi_{\rm lab}$ from the center of a given sector. Due to the hyperbolic geometry of CLAS and the presence of a toroidal magnetic field, the fiducial boundaries of $\phi_{\rm lab}$ are functions of a track's momentum, charge, and polar angle. Moreover, events were removed from this analysis if the primary interaction z-vertex was very close to the downstream boundary of the liquid-hydrogen target. The z-vertex resolution was dependent on the track angle and best for tracks that were perpendicular to the beam axis. In this experiment, the upstream shift of the long target cell from the center of the CLAS spectrometer affected the reconstructed upstream and downstream edges of the z-vertex distribution differently. Figure 4 shows that the downstream region could

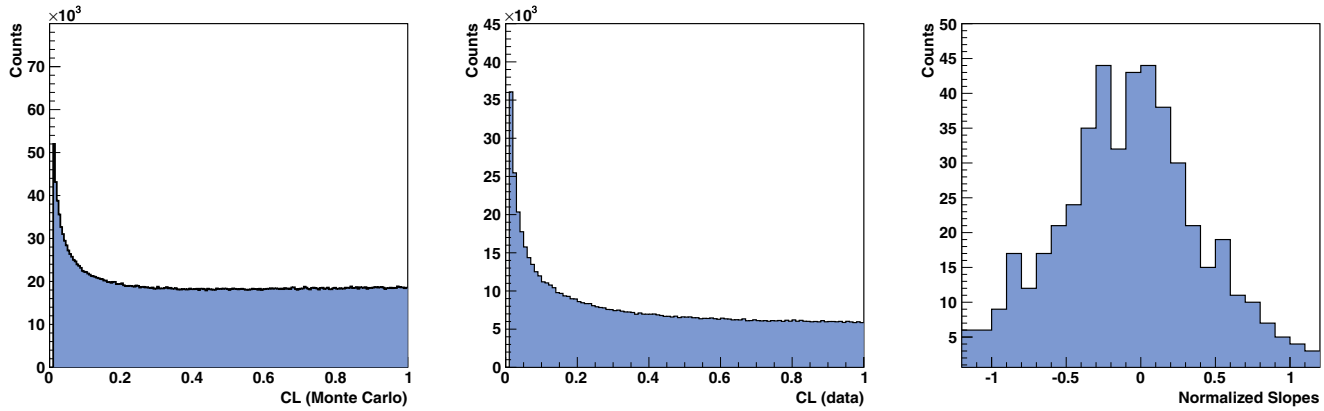

FIG. 6. Confidence-level distribution for the missing-π^0 hypothesis after all corrections for Monte Carlo (MC) events (left) and CLAS-g12 data (center). The covariance matrix for both data and MC events was initially tuned using fully exclusive $\gamma p \to p\pi^+\pi^-$ events. Right: Distribution of normalized slopes for data events, see text for more details.

not be sufficiently well reproduced in the Monte Carlo simulations. Therefore, a cut of -110 cm $< z$-vertex < -72 cm was applied to the final event sample.

The exclusive $p\pi^+\pi^-$ channel was identified as a dominant background source. This charged double-pion reaction has a significantly larger cross section than any other competing reaction leading to an additional π^0 meson in the final state. In this analysis, $p\pi^+\pi^-$ leakage into the selected $p\pi^+\pi^-$ (π^0) data sample was observed due to the relatively small difference in the missing masses of these two final states. If an incorrect initial-state photon candidate was selected with an energy higher than the correct incident photon, then this additional energy and z-momentum would allow for the reconstruction of an artificial π^0 in the final state that would move along the incident photon-beam direction. Therefore, leakage from the $\gamma p \to p\pi^+\pi^-$ channel was observed as an excess of π^0 mesons in the very forward direction. To reduce the contribution from $\gamma p \to p\pi^+\pi^-$ background, only events with $\cos\theta^{\pi^0}_{\text{c.m.}} < 0.99$ were retained for further analysis.

In a final step, all events were subject to kinematic fitting. Events were tested separately for energy and momentum conservation in a four-constraint (4C) fit to identify the reaction $\gamma p \to p\pi^+\pi^-$ and in a one-constraint (1C) fit to test for a missing π^0. Three pieces of information are needed for a missing particle. The missing four-momentum initially introduces four additional unknown parameters. However, the particle's energy and momentum are related by the invariant mass. Since energy and momentum conservation provides four constraints, the missing-particle hypothesis reduces to a one-constraint fit. The exclusive reaction $\gamma p \to p\pi^+\pi^-$ was used to tune the covariance matrix with a set of common parameters that have also been applied in other CLAS-g12 analyses involving kinematic fitting. This procedure secures Gaussian pull distributions and a flat confidence-level (CL) distribution, where the CL denotes the *goodness of fit* of the statistical model applied to the data and is defined as the integral over the χ^2 probability density function in the range $[\chi^2, \infty]$ [61].

Figure 6 (center) shows the confidence-level distribution for the missing-π^0 hypothesis after all corrections; the distribution is fairly flat. In addition to the quality of the global CL and pull distributions, the flat shape of the CL distributions was also checked in all relevant kinematic regions by considering the *normalized slope* of each distribution:

$$\bar{a} = \frac{a}{a/2 + b}, \tag{4}$$

where a is the slope and b is the y intercept obtained by fitting a first-order polynomial to the confidence-level distribution on the interval [0.6, 1.0]. Figure 6 (right) shows the respective normalized slopes integrated over all analyzed energies and η center-of-mass angles. The distribution is symmetric and centered at *zero* demonstrating the relative flatness of the CL distributions in all kinematic bins and thus, the good understanding of the measurement uncertainties. Events in this analysis were retained with a confidence-level cut of $p > 0.01$.

Figure 7 shows the missing mass using nonkinematically fitted four-vectors in the reaction $\gamma p \to p\eta \to p\pi^+\pi^-(X)$, integrated over all available incident photon energies, after all cuts and the final η background subtraction described in the following section. A clean π^0 peak is visible with a Gaussian width of $\sigma = 17.0$ MeV.

C. Monte Carlo simulations

The performance of the experimental setup was studied in GEANT3-based [62] Monte-Carlo (MC) simulations. The acceptance for the reaction $\gamma p \to p\eta \to p\pi^+\pi^-\pi^0$ was determined by generating events, which were evenly distributed across the available phase space. The MC events were then analyzed using the same reconstruction and selection criteria, which were applied to the measured data events. The simulated tracks were corrected for the energy loss along their trajectories but were not subject to any momentum corrections since all the DC components were perfectly positioned in the simulations and a homogeneous magnetic field was used. The same hypotheses were tested in the kinematic fits and events selected with the same confidence level cut. The acceptance for each kinematic bin was then defined as the ratio of the

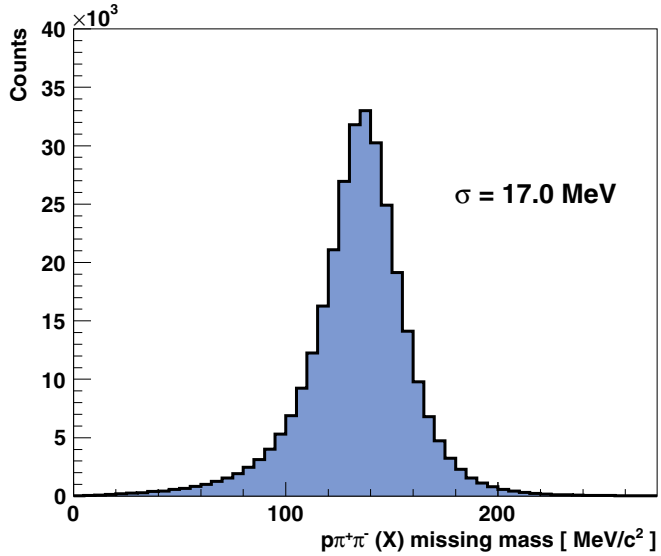

FIG. 7. Missing mass X in the reaction $\gamma p \to p\eta \to p\pi^+\pi^-(X)$ after all cuts and the final η background subtraction. A clean π^0 peak is visible.

number of generated to reconstructed MC events:

$$A_{\gamma p \to p\eta} = \frac{N_{\text{rec, MC}}}{N_{\text{gen, MC}}}. \tag{5}$$

In the real CLAS-g12 data, information about the trigger condition was encoded in the so-called trigger word, which was available in the data stream for every event. The overall trigger (in)efficiency was evaluated by studying the efficiency of individual charged tracks to produce a trigger-level signal in a sample of exclusive $\gamma p \to p\pi^+\pi^-$ events, where each final-state particle was detected in a different sector of CLAS. Since one of the trigger conditions required only (at least) two charged tracks in two different sectors (see Sec. III E), any inefficiencies could be studied by comparing with the encoded trigger information. The trigger efficiency for a charged track was then given as the fraction of events where a third particle could be reconstructed in a different sector but the information was not recorded in the corresponding trigger bit. Trigger efficiency maps were developed for each particle type (proton, π^+, π^-) as a function of sector ID, TOF counter, and azimuthal angle, ϕ. The average CLAS-g12 efficiency values for the proton, π^+, and π^- are 0.89, 0.83, and 0.75, respectively. These maps were applied in the Monte Carlo simulations by generating a random number for each track and removing the track if the random number exceeded the corresponding efficiency stored in the map.

D. Background subtraction

In the determination of the η photoproduction cross sections reported here, nonsignal background events were removed in a probabilistic event-based approach called the "Q-factor method," which is fully described in Ref. [63]. A brief summary of the method and its application to the data from CLAS-g12 is given in this section.

For every event in this analysis, a quality factor (or Q value) was determined that describes the probability for an event to be a signal event as opposed to background. The approach used the unbinned maximum-likelihood technique. For every selected $\gamma p \to p\eta$ event and its N_c kinematically nearest neighbors, the following function was fit to the invariant $M_{\pi^+\pi^-\pi^0}$ mass distribution:

$$f(x) = N \cdot [f_s \cdot S(x) + (1 - f_s) \cdot B(x)], \tag{6}$$

where $S(x)$ and $B(x)$ denote the signal and the background probability density functions, respectively, and $x = M_{\pi^+\pi^-\pi^0}$. A double-Gaussian profile was chosen for the signal and the background shape was modeled with a second-order Chebyshev polynomial. The parameter N in Eq. (6) is a normalization constant and f_s is the signal fraction with a value between 0 and 1.

The kinematically nearest neighbor events were selected by defining a distance metric for the phase space spanned by a set of kinematic variables O_k. These independent quantities were chosen to be

$$\cos\theta^{\eta}_{\text{c.m.}},\ \cos\theta_{\text{HEL}},\ \phi_{\text{HEL}},\ \phi^{\eta}_{\text{lab}},\ \lambda, \tag{7}$$

where $\cos\theta^{\eta}_{\text{c.m.}}$ denotes the cosine of the polar angle of the η in the center-of-mass frame, $\cos\theta_{\text{HEL}}$ and ϕ_{HEL} describe the orientation of the η decay plane in the helicity frame, and $\phi^{\eta}_{\text{laboratory}}$ is the azimuthal angle of the η in the laboratory frame. The variable $\lambda = |\vec{p}_{\pi^+} \times \vec{p}_{\pi^-}|^2 / \lambda_{\max}$ is defined in terms of the pion momenta in the η rest frame and is proportional to the $\eta \to \pi^+\pi^-\pi^0$ decay amplitude as a consequence of isospin conservation [64], with $\lambda_{\max}$ defined as [65]

$$\lambda_{\max} = K^2\left(\frac{K^2}{108} + \frac{mK}{9} + \frac{m^2}{3}\right), \tag{8}$$

for a totally symmetric decay, where $K = T_1 + T_2 + T_3$ is the sum of the $\pi^{\pm,0}$ kinetic energies and m is the $\pi^{\pm}$ mass.

Initially defined for vector mesons, λ has a limited physics interpretation for pseudoscalar mesons but still serves as an independent kinematic variable in this analysis. The background subtraction described in this section was performed simultaneously for the ω and η meson decaying to the same $\pi^+\pi^-\pi^0$ final state. Results on cross section measurements for $\gamma p \to p\omega$ will be presented in a forthcoming publication [66]. The parameter λ varies between 0 and 1 and the number of events as a function of λ shows a linearly increasing behavior for vector mesons, whereas a flat distribution is expected for the η meson. This is nicely observed in Fig. 8. Using the quantities listed in Eq. (7), the kinematic distance between two events i and j is defined as

$$d^2_{ij} = \sum_{k=1}^{5}\left(\frac{O^i_k - O^j_k}{\Delta_k}\right)^2, \tag{9}$$

where the O_k denotes the set of kinematic variables for the two events i and j, and Δ_k is the full range for the kinematic variable k.

The Q value for a selected $\gamma p \to p\eta$ event is finally given as the signal component at the event's invariant $\pi^+\pi^-\pi^0$ mass in the overall mass distribution of the event and its $N_c = 500$

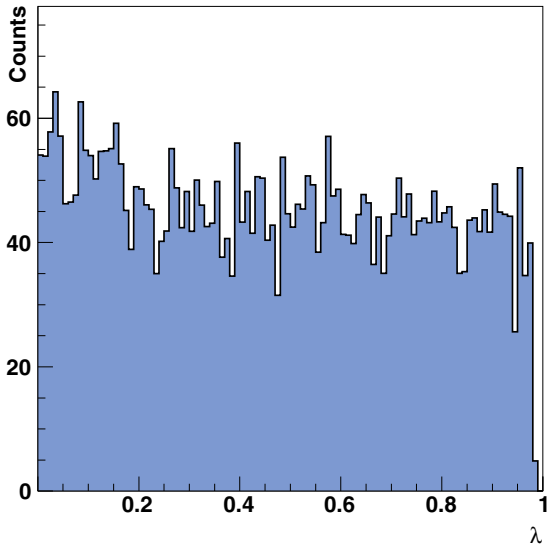

FIG. 8. Typical example of a normalized $\lambda = |\vec{p}_{\pi^+} \times \vec{p}_{\pi^-}|^2$ distribution for the center-of-mass energy bin $W \in [2360,\ 2400]$ MeV.

nearest neighbors:

$$Q = \frac{s(x)}{s(x) + b(x)}, \tag{10}$$

where x is again the invariant mass of the $\pi^+\pi^-\pi^0$ system, $s(x) = f_s S(x)$, and $b(x) = (1 - f_s)B(x)$ [see also Eq. (6)].

The Q values were then used as weight factors for various kinematic distributions in this analysis. Figure 9 shows examples of the resulting separation of signal and background in the invariant $\pi^+\pi^-\pi^0$ mass distribution. Three angle bins are presented in the energy range $W \in [1.90,\ 1.92]$ GeV. The sum of the signal (white area) and the background (blue area) is identical to the total unweighted mass distribution, whereas the invariant 3π mass of each event weighted by $1 - Q$ gives the background alone. Figure 10 shows the total invariant $\pi^+\pi^-\pi^0$ mass distribution for the energy range $W \in [1.76,\ 2.36]$ GeV representing the underlying event statistics in Figs. 11–15. An excellent signal/background separation is observed with ≈269 000 η events in the signal peak.

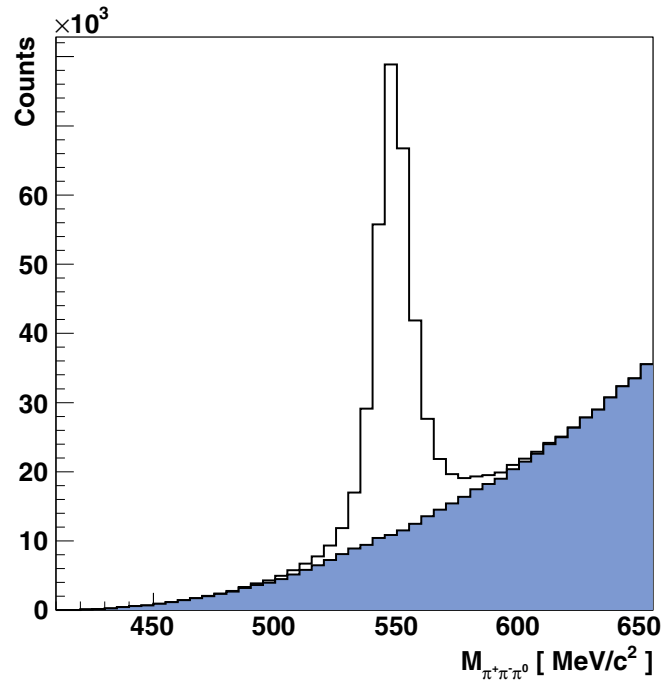

FIG. 10. Total invariant $\pi^+\pi^-\pi^0$ mass distribution for the center-of-mass energy $W \in [1.76,\ 2.36]$ GeV corresponding to the combined $\gamma p \to p\eta$ event statistics of Figs. 11–15.

V. EXTRACTION OF CROSS SECTIONS

The differential cross sections, $d\sigma/d\Omega$, for the reaction $\gamma p \to p\eta$ are determined according to

$$\frac{d\sigma}{d\Omega} = \frac{N_{\gamma p \to p\eta}}{A_{\gamma p \to p\eta}} \frac{1}{N_\gamma\, \rho_{\text{target}}} \frac{1}{\Delta\Omega} \frac{1}{\text{BR}}, \tag{11}$$

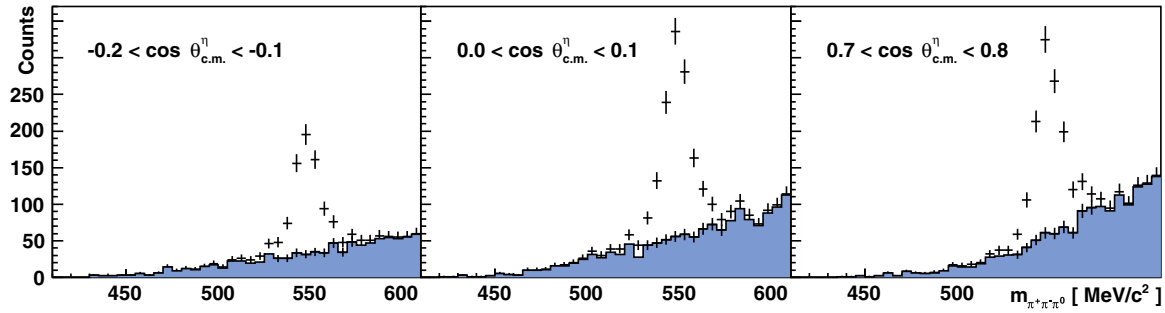

FIG. 9. Examples of $\pi^+\pi^-\pi^0$ mass distributions for the center-of-mass energy range $W \in [1.90,\ 1.92]$ GeV for events that were subject to the Q-factor fitting (background subtraction). These events survived all kinematic cuts. The invariant 3π mass of each event weighted by $1 - Q$ gives the blue area (background), whereas the signal peak comes from the invariant mass weighted by Q.

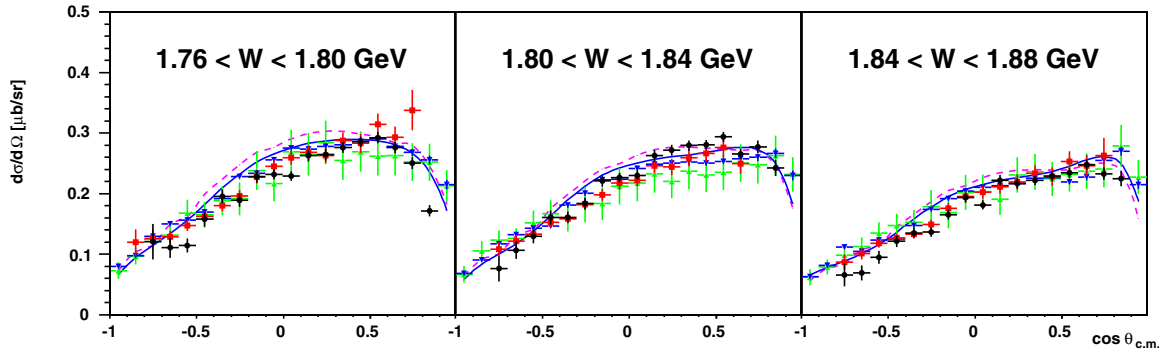

FIG. 11. The differential cross sections $d\sigma/d\Omega$ for three 40-MeV-wide center-of-mass energy W bins. The new CLAS data are shown as the black solid circles (●) and the uncertainties associated with each point comprise the statistical uncertainty and contributions from the Q-value correlation uncertainty added in quadrature. Also shown for comparison are data from CLAS-g11a [30] (■), the A2 Collaboration at MAMI [33] (▼) using their published center-of-bin energies of $W = 1.78$ GeV (left), 1.82 GeV (center), 1.86 GeV (right), and the CBELSA/TAPS Collaboration at ELSA [31] (▲). The blue solid and purple dashed curves denote the η-MAID 2018 [4] and the BnGa 2019 [21] description of the $\gamma p \to p\eta$ cross section, respectively.

where

ρ_{target}: target area density
$N_{\gamma p \to p\eta}$: number of reconstructed signal events in a (W, $\cos\theta_{\text{c.m.}}$) bin
N_γ: number of photons in an incident E_γ bin
$A_{\gamma p \to p\eta}$: acceptance in a (W, $\cos\theta_{\text{c.m.}}$) bin
$\Delta\Omega$: solid-angle interval $\Delta\Omega = 2\pi\,\Delta\cos(\theta_{\text{c.m.}})$
BR: decay branching fraction.

The target area density, i.e., the number of atoms in the target material per cross-sectional area (orthogonal to the photon beam), is given by

$$\rho_{\text{target}} = 2\,\frac{\rho(\text{H}_2)\,N_A\,L}{M_{\text{mol}}(\text{H}_2)} = 16.992\times10^{-7}\mu\text{b}^{-1}, \qquad (12)$$

where $\rho(\text{H}_2) = 0.0711$ g/cm^3 [59] is the average density, $M_{\text{mol}} = 2.01588$ g/mol is the molar mass of liquid H_2, and $L = 40.0$ cm is the length of the CLAS-g12 target cell. Finally, $N_A = 6.022\times10^{23}$ mol^{-1} is Avogadro's number. The factor of two accounts for the molecular composition of hydrogen (H_2).

The solid angle in steradians equals the area of a segment of a unit sphere. The full solid angle of a sphere measured from any point in its interior is thus $2\times2\pi = 4\pi$ sr, where 2π originates from integrating over the azimuthal angle and the factor of two from integrating over $\sin\theta\,d\theta$ (polar angle). Since the differential cross sections are integrated over ϕ_{lab} but are binned in $\cos\theta_{\text{c.m.}}$, $\Delta\Omega = 2\pi\,\Delta\cos(\theta_{\text{c.m.}})$ was used in Eq. (11) and $\Delta\cos(\theta_{\text{c.m.}}) = 2$ / (# of angle bins). In this analysis, the available statistics allowed for 20 angle bins and thus, $\Delta\Omega = 0.6283$.

The branching fraction for the charged decay mode $\eta \to \pi^+\pi^-\pi^0$ of $\Gamma_{\pi^+\pi^-\pi^0}/\Gamma = (22.92\pm0.28)\%$ was taken from Ref. [22], where $\Gamma = (1.31\pm0.05)$ keV [22].

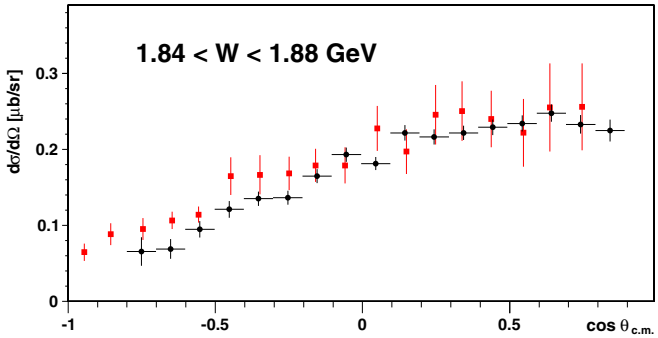

FIG. 12. The differential cross sections $d\sigma/d\Omega$ for the energy bin $1.84 < W < 1.88$ GeV. The new CLAS data are shown as the black solid circles (●) and the uncertainties associated with each point comprise the statistical uncertainty and contributions from the Q-value correlation uncertainty added in quadrature. Also shown for comparison are data from the GRAAL Collaboration [16] (■).

A. Normalization

The photon flux for the absolute normalization of the extracted differential cross sections was determined using

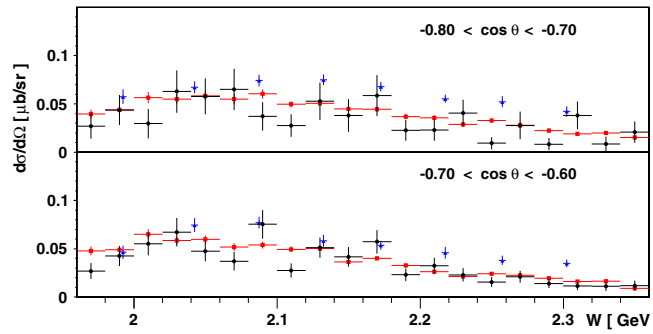

FIG. 13. The differential cross sections $d\sigma/d\Omega$ for the backward angle bins $-0.8 < \cos\theta < -0.7$ (top) and $-0.7 < \cos\theta < -0.6$ (bottom). The new CLAS data are shown as the black solid circles (●) and the uncertainties associated with each point comprise the statistical uncertainty and contributions from the Q-value correlation uncertainty added in quadrature. Also shown for comparison are data from CLAS-g11a [30] (■) and from the LEPS Collaboration [27] (▲).

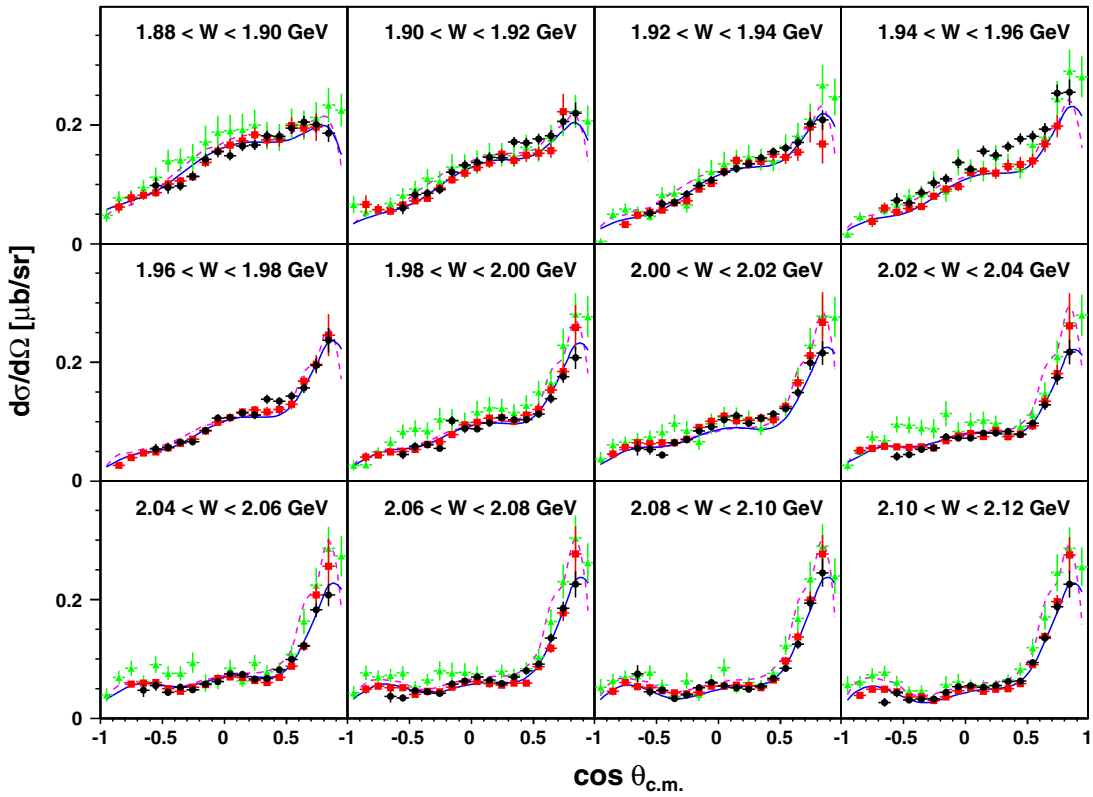

FIG. 14. The differential cross sections $d\sigma/d\Omega$ in 20-MeV-wide center-of-mass bins for $W \in [1.88,\ 2.12]$ GeV. The new CLAS data are shown as the black solid circles (●) and the uncertainties associated with each point comprise the statistical uncertainty and contributions from the Q-value correlation uncertainty added in quadrature. Also shown for comparison are data from CLAS-g11a [30] (■) and from the CBELSA/TAPS Collaboration at ELSA [31] (▲). The blue solid and purple dashed curves denote the η-MAID 2018 [4] and the BnGa 2019 [21] description of the $\gamma p \to p\eta$ cross section, respectively.

standard CLAS procedures. The method is described in Ref. [67] and based on comparing the number of "good" electrons in the tagger with the number of photons traversing the liquid-hydrogen target measured with a total absorption counter (TAC) placed directly in the photon beam. Such normalization runs were carried out at about 10% of the production beam current using a thinner bremsstrahlung radiator to determine the tagging ratio ϵ^{T} of each T-counter. The tagging ratio is given by the ratio of "good" tagger hits in coincidence with the TAC to the total number of "good" hits in the tagger and is approximately between 75% and 80%. Photons can be lost on the way from the tagger to the target due to dispersion of the beam, collimation, and Møller scattering, for instance. The number of "good" electrons is given by integrating the observed electron rates at the tagger over the data acquisition (DAQ) live time of the experiment, which is measured with a clock. The number of tagged photons per T-counter is then given by

$$N_{\gamma}^{\mathrm{T}} = \frac{N_{\mathrm{e}^-}^{\mathrm{T}} \times \epsilon^{\mathrm{T}}}{1 - \alpha}, \tag{13}$$

where $N_{\mathrm{e}^-}^{\mathrm{T}}$ is the number "good" electrons per T-counter and the photon attenuation factor, α, denotes the small fractional loss of photons from the liquid-hydrogen target to the TAC.

B. Systematic uncertainties

The statistical uncertainties were determined from the number of $p\eta$ events in each $(W, \cos\theta_{\mathrm{c.m.}}^{\eta})$ or $(W, -t)$ bin, and are included in the uncertainties shown for all data points. In this analysis, the effective number of events in each kinematic bin was given by summing over all Q values of the contributing events.

The overall systematic uncertainty includes uncertainties in the normalization, as well as contributions from reconstruction-related sources and the background-subtraction method. An overview of the different fractional contributions (% uncertainties) is given in Table II. These contributions are not included in the following results figures. A brief discussion of the contribution from the background-subtraction method is given in this section below. Such contributions are included in the uncertainty shown for each data point (added in quadrature to the statistical uncertainty).

An individual event's Q value is based on a fit to the invariant $\pi^+\pi^-\pi^0$ mass distribution that is formed by the event and its kinematically nearest neighbors using the maximum-likelihood technique. The covariance matrix, C_{η}, for the set of fit parameters, $\vec{\eta}$, was used to determine the uncertainty of the

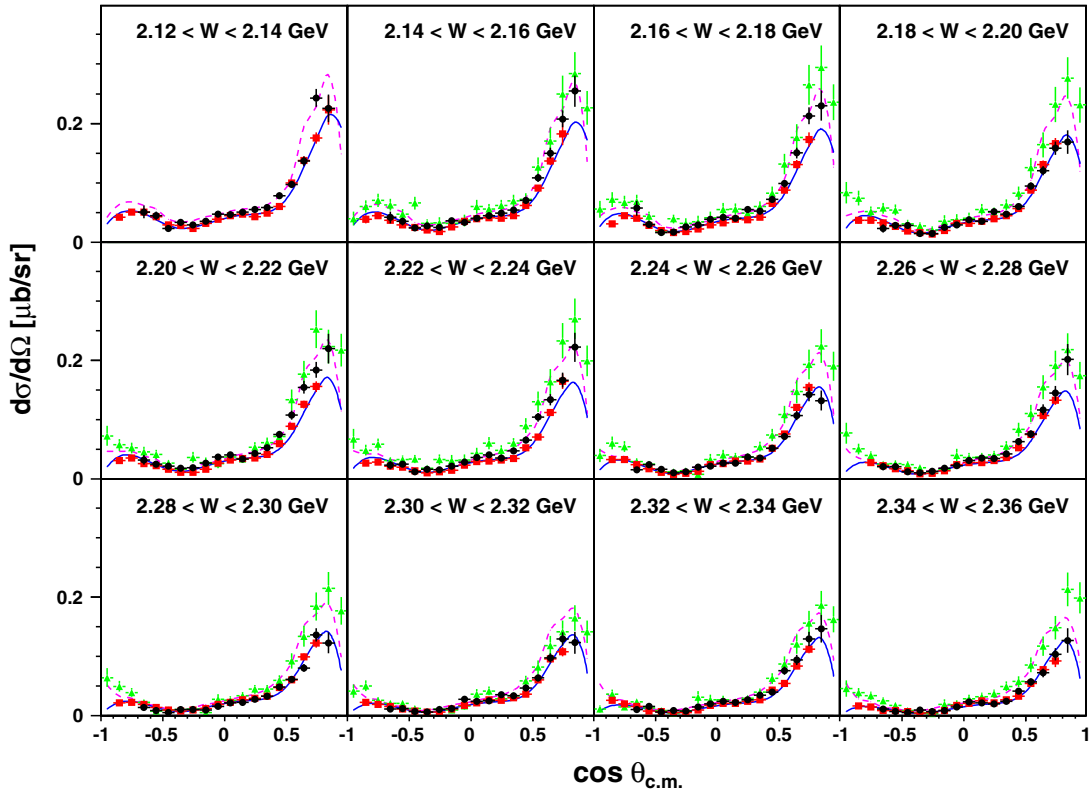

FIG. 15. The differential cross sections $d\sigma/d\Omega$ in 20-MeV-wide center-of-mass bins for $W \in [2.12,\ 2.36]$ GeV. The new CLAS data are shown as the black solid circles (•) and the uncertainties associated with each point comprise the statistical uncertainty and contributions from the Q-value correlation uncertainty added in quadrature. Also shown for comparison are data from CLAS-g11a [30] (■) and from the CBELSA/TAPS Collaboration at ELSA [31] (▲). The blue solid and purple dashed curves denote the η-MAID 2018 [4] and the BnGa 2019 [21] description of the $\gamma p \to p\eta$ cross section, respectively.

Q value for the given event:

$$\sigma_Q^2 = \sum_{k,\,m} \frac{\partial Q}{\partial \eta_k} \left(C_\eta^{-1}\right) \frac{\partial Q}{\partial \eta_m}\,, \tag{14}$$

where the summation runs over all signal and background parameters used in the total fit function $f(x)$, which is defined in Eq. (6).

The Q factor method naturally led to some correlations among events and their nearest neighbors because events could serve as neighbors for many *seed* events. The systematic "correlation" uncertainty of the η yield in each kinematic bin due to the method as such was given by

$$\sigma_\eta^2 = \sum_{i,\,j} \sigma_Q^i\, \rho_{ij}\, \sigma_Q^j, \tag{15}$$

where the sum i, j was taken over all the events in the kinematic bin, σ_Q^i and σ_Q^j denote the fit uncertainties for events i and j, and ρ_{ij} represents the correlation factor between events i and j. The correlation factor is simply the fraction of shared nearest-neighbor events and a number between *zero* and *one*. In high-statistics event samples, the correlation among events is typically small and the corresponding contribution to the overall systematic uncertainty is negligible, whereas in low-statistics samples, the contribution can quickly exceed the basic statistical uncertainty.

The contribution from the Q-factor method was then added to the statistical uncertainty in quadrature to obtain the total "statistics-based" uncertainty that is shown for each data point in subsequent figures:

$$\sigma^2 = \sigma_\eta^2 + \sigma_{\text{statistical}}^2. \tag{16}$$

An additional CL cut of $p > 0.05$ was examined and the resulting differential cross sections were compared with the original results when a nominal cut of just $p > 0.01$ was used. Both the difference and ratio distributions were observed to be symmetric and Gaussian reflecting a change in the results,

TABLE II. Summary of the fractional contributions to the overall systematic uncertainty.

Source of uncertainty	% Uncertainty
Sector-by-sector relative acceptance [59]	5.9
Fiducial cuts	2.5
z-vertex cut	2.6
Upstream / downstream target half	1.5
Kinematic fitting (CL cut)	1.6
Trigger efficiency correction	1.1
Liquid-hydrogen target [59]	0.5
Normalization (photon flux) [59]	5.7
Branching fraction ($\eta \to \pi^+\pi^-\pi^0$)	0.28

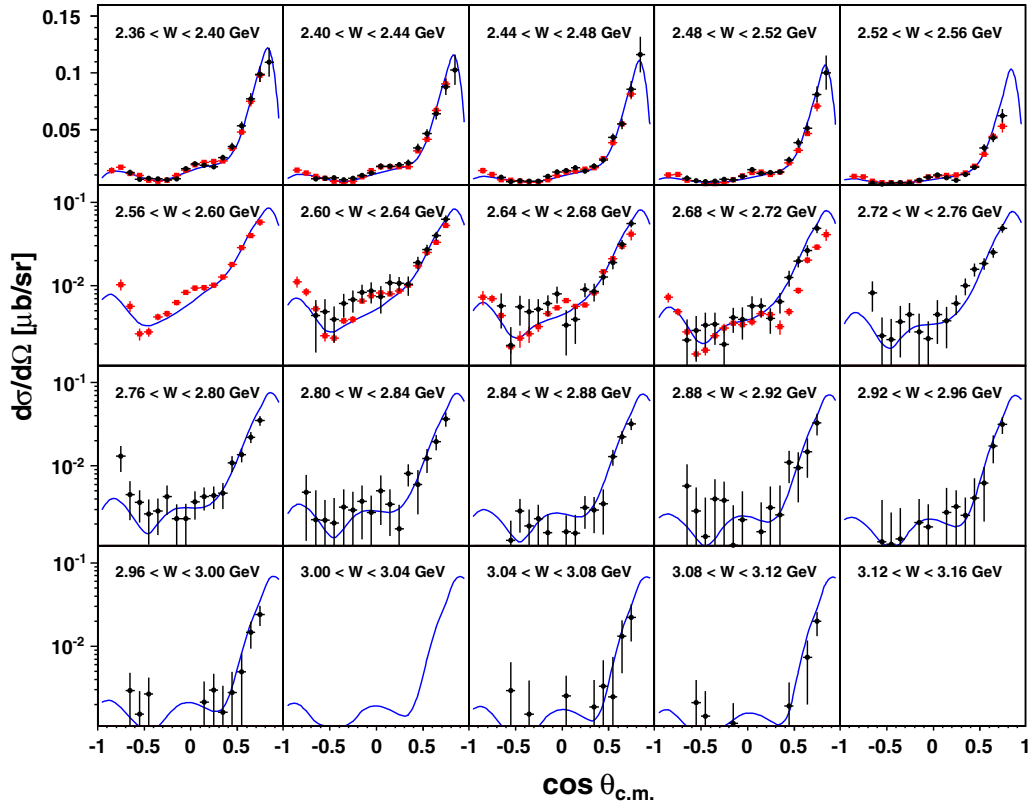

FIG. 16. The differential cross sections $d\sigma/d\Omega$ in 40-MeV-wide center-of-mass bins for $W \in [2.36,\ 3.12]$ GeV. The new CLAS data are shown as black solid circles (●) and the uncertainties associated with each point comprise the statistical uncertainty and contributions from the Q-value correlation uncertainty added in quadrature. Also shown for comparison are data from CLAS-g11a [30] (■). The blue solid curve denotes the η-MAID 2018 [4] description of the $\gamma p \to p\eta$ cross section.

which is mostly statistical in nature due to the loss of events when using a larger p value. A possible contribution from the different slopes of the z-vertex distributions in data and Monte Carlo (observed in Fig. 4) was studied by comparing the differential cross section results based on events which originated from either the upstream or downstream half of the liquid hydrogen target. The ratio distribution was found to be symmetric, but shifted away from unity by about 1.5%. Finally, this analysis was also repeated without any z-vertex cut. A Gaussian fit to the corresponding (very narrow and symmetric) ratio distribution resulted in a small shift of 2.6%.

In the ideal CLAS-g12 experiment, the detector response will be the same in each of the six CLAS sectors. However, a contribution to the overall systematic uncertainty can arise from small sector-by-sector relative acceptance effects. To quantify such a contribution, acceptance-corrected event yields were determined for each sector and compared with the average for all six sectors [59]. The resulting sector-by-sector systematic uncertainty of 5.9% was found to be consistent with the systematic uncertainty quoted for CLAS-g11a [30]. The trigger efficiency maps discussed in Sec. IV C were functions of only sector-related quantities. Therefore, the same uncertainty of 5.9% was considered for the average trigger efficiency correction of about 18%.

The contribution from the liquid hydrogen target to the overall systematic uncertainty accounts for effects such as the contraction, length, etc. Previous CLAS experiments have determined that the effect is approximately at the 0.5% level [59]. Finally, the systematic uncertainty associated with the incident-photon flux normalization was estimated by studying the distribution of flux-normalized event yields for all production runs at different electron-beam currents [59].

VI. EXPERIMENTAL RESULTS

The cross section data presented in this section have been analyzed by varying the energy-bin width in three different energy ranges to adjust for the available statistics in this experiment and to facilitate the comparison with other published data. Differential cross sections in terms of $d\sigma/d\Omega$ are shown for all energies in Figs. 11–17. Representations in terms of W and momentum transfer $-t$ are given in Figs. 18–20. The uncertainty associated with each data point comprises contributions from the statistical uncertainty and the Q-value correlation uncertainty added in quadrature.

A. Differential cross sections $d\sigma/d\Omega$

Figure 11 shows the differential cross sections $d\sigma/d\Omega$ for the W range [1.76, 1.88] GeV in 40-MeV-wide energy bins and 0.1-wide angle bins in $\cos\theta^{\eta}_{\rm c.m.}$ of the η meson in the center-of-mass frame. The CLAS-g12 data are given as the

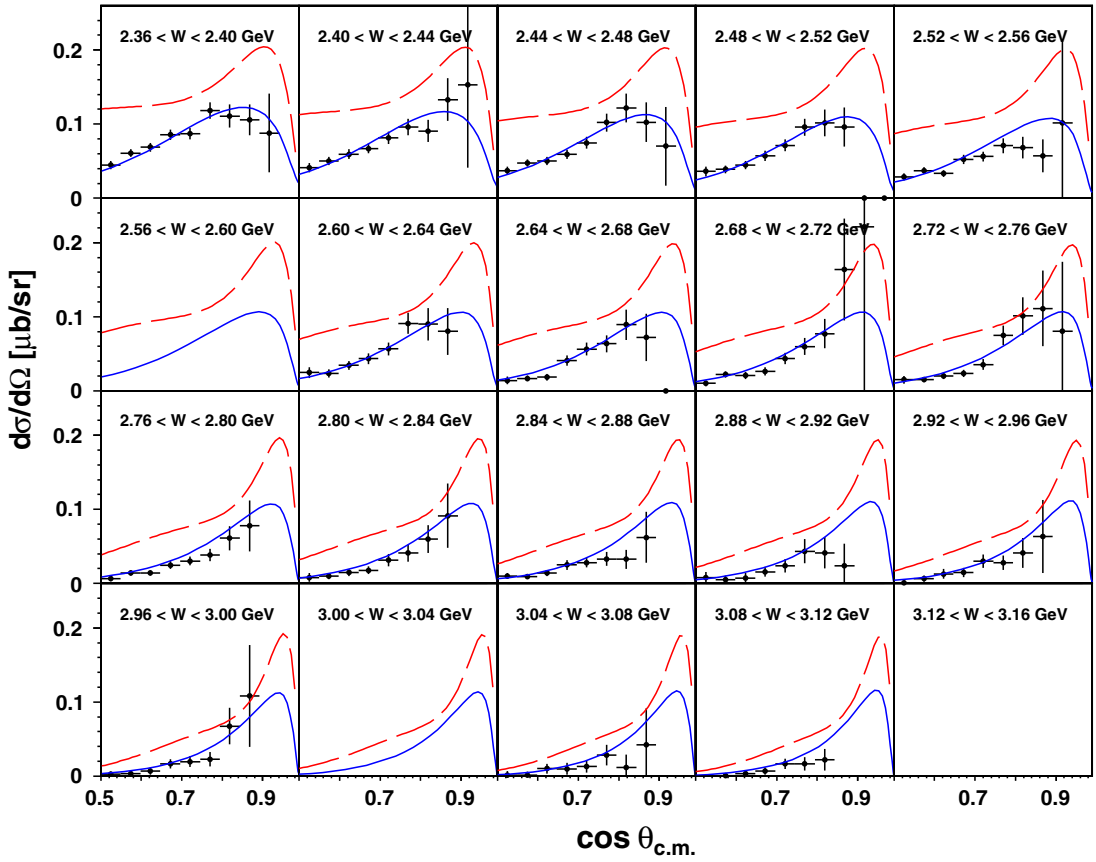

FIG. 17. The differential cross sections $d\sigma/d\Omega$ in 40-MeV-wide center-of-mass bins for $W \in [2.36, 3.12]$ GeV and just the forward direction $\cos\theta^{\eta}_{\text{c.m.}} > 0.5$. The new CLAS data are shown as the black solid circles (•) and the uncertainties associated with each point are comprised of the statistical uncertainty and contributions from the Q-value correlation uncertainty added in quadrature. The blue solid curve denotes the η-MAID 2018 description [4] of the $\gamma p \to p\eta$ cross section, whereas the red long-dashed curve represents the Regge model discussed in Ref. [3].

black data points. For comparison, the distributions also show the earlier published CLAS-g11a data [30] as the red points. These data are available in 20-MeV-wide energy bins and therefore, adjacent bins were averaged. The agreement is very good within the given uncertainties. Moreover, data from the A2 Collaboration at MAMI [33] are shown as the blue points with the published center-of-bin W energy closest to any of the center-of-bin energies presented in the figure. The overall agreement is good. Finally, data from CBELSA/TAPS [31] are given as the green points. Again, the overall agreement of all four data sets ranges from fair to very good. Some discrepancies can be attributed to small energy mismatches in the presentation of the data. The CLAS-g12 data tend to be systematically lower in the backward direction for $\cos\theta^{\eta}_{\text{c.m.}} < -0.5$. A possible explanation is the poor CLAS acceptance in this kinematic range since the target was significantly shifted upstream for this experiment. The A2 and CBELSA/TAPS data seem to slightly underestimate the CLAS data in the forward direction for $1.80 < W < 1.84$ GeV. However, no significant normalization discrepancy is observed in any of these W bins.

Figure 12 shows a comparison of the new CLAS data (black points) with previous results from the GRAAL Collaboration [16] (red points) for the center-of-mass energy bin $1.84 < W < 1.88$ GeV. The agreement is excellent in the forward direction and no overall normalization discrepancy is observed. However, the CLAS-g12 data are again found to be slightly lower in the backward direction for $\cos\theta^{\eta}_{\text{c.m.}} < -0.2$.

The set of angular distributions for the energy range $W \in [1.88, 2.36]$ GeV corresponding to the incident photon energy $E_\gamma \in [1.41, 2.50]$ GeV is shown in Figs. 14 and 15 in 20-MeV-wide W bins and 0.1-wide angle bins in $\cos\theta^{\eta}_{\text{c.m.}}$. For comparison, as before, the CLAS-g11a [30] and CBELSA/TAPS [31] data are also shown; MAMI data are only available below $E_\gamma < 1.45$ GeV and therefore, are not included in these figures. The earlier CLAS data have not been averaged for these distributions since they were published in 20-MeV-wide bins. While the agreement of the two CLAS data sets is excellent, the CBELSA/TAPS data tend to be systematically higher. The CBELSA/TAPS data had to be converted to W bins and for this reason, some discrepancies can be explained in terms of small energy mismatches. Nevertheless, the ELSA data seem to be systematically higher especially in the very forward and backward direction above $E_\gamma \approx 2.0$ GeV or $W \approx 2.2$ GeV. This observation was already discussed in Refs. [30,31] and was also reported for other reactions, e.g., in ω photoproduction [68]. The latter suggests an energy-dependent normalization issue of unknown nature

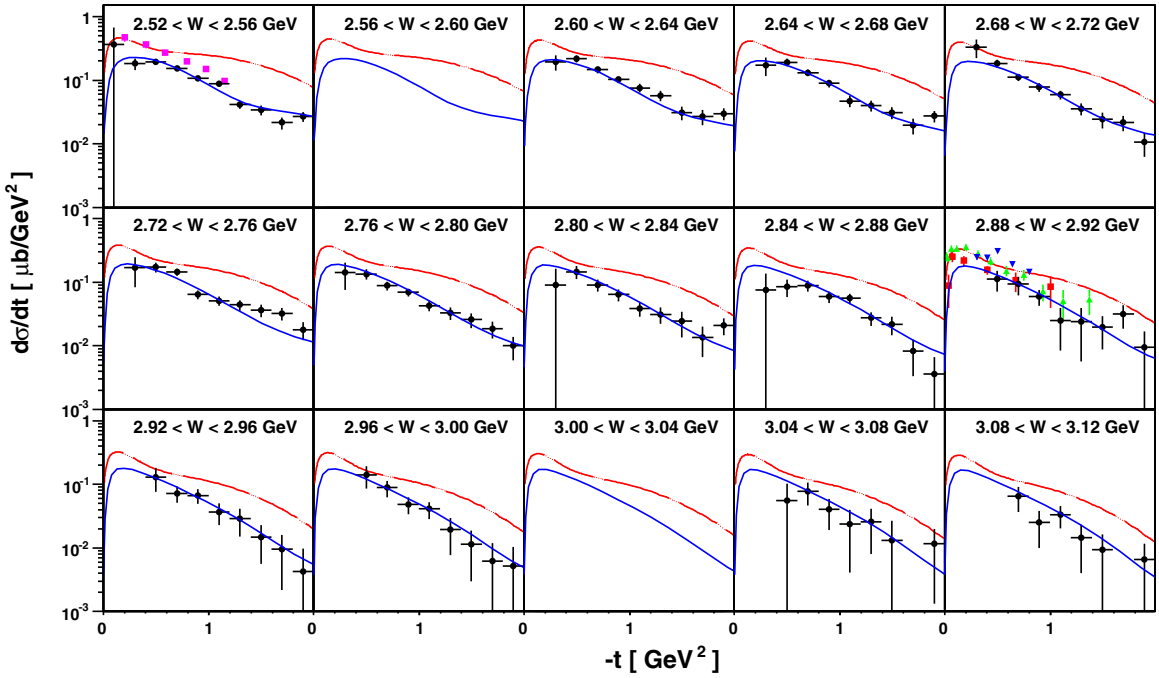

FIG. 18. The differential cross sections $d\sigma/dt$ in 40-MeV-wide center-of-mass bins for $W \in [2.52, 3.12]$ GeV and for the $-t$ range [0, 2] GeV^2. The new CLAS data are shown as the black solid circles (●) and the uncertainties associated with each point are comprised of the statistical uncertainty and contributions from the Q-value correlation uncertainty added in quadrature. In the energy range $2.52 < W < 2.56$ GeV, data from NINA at the Daresbury Laboratory [35] (■) are given for comparison. And in the energy range $2.88 < W < 2.92$ GeV, also shown are data from DESY [36] (▲), MIT [38] (■), and Cornell [39] (▼). The red long-dashed curve represents the Regge model discussed in Ref. [3] and the blue solid curve denotes the η-MAID 2018 description [4].

but it is also worth emphasizing that the calorimeter-based CBELSA/TAPS experimental setup has better acceptance in the very forward direction. Given the excellent agreement of the two CLAS data sets, the reason for this discrepancy remains unclear, though.

The shapes of the angular distributions are indicative of nucleon resonance production in the entire energy range presented in Figs. 14 and 15. Moreover, the very prominent forward-peaking develops around and above $W \approx 1.96$ GeV, which suggests that t-channel processes become increasingly relevant.

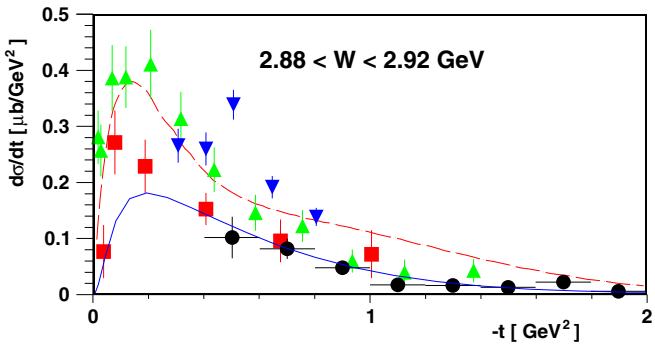

FIG. 19. The differential cross section $d\sigma/dt$ for $W \in [2.88, 2.92]$ GeV and for the $-t$ range [0, 2] GeV^2 using a linear scale. For the color code and an explanation of the curves, see the caption of Fig. 18.

Figure 13 shows the energy dependence of these new CLAS data (black points) for two backward angle bins in comparison with results from CLAS-g11a [30] (red points) and from the LEPS Collaboration [27] (blue points). Note that the acceptance of this CLAS experiment was significantly reduced in the backward direction since the liquid hydrogen target was moved upstream. The agreement between the two CLAS data sets within their respective uncertainties is excellent, though. The SPring-8/LEPS facility has also better acceptance for the detection of mesons in the backward direction. In comparison, the LEPS data points are observed to be higher than the CLAS points for the entire energy range shown in the figure. Moreover, the LEPS data in Fig. 13 indicate the presence of a bump structure around $W \approx 2.1$ GeV. In Ref. [27], the authors claim that a contribution from nucleon resonances is needed to explain this structure. Both CLAS data sets are consistent with the presence of this bump structure. However, the CLAS-g12 acceptance and the available statistics in this kinematic region does not facilitate further studies into the nature of the bump.

Finally, differential cross section results for the energy range $W \in [2.36, 3.12]$ GeV corresponding to incident photon energy $E_\gamma \in [2.50, 4.71]$ GeV are shown in Fig. 16 in 40-MeV-wide W bins and 0.1-wide angle bins in $\cos\theta^\eta_{\text{c.m.}}$. Note that the vertical axis switches from a linear to a logarithmic scale for $W > 2.56$ GeV (second row), seemingly changing the shape of the angular distributions and visibly increasing the reported uncertainties. The agreement with the

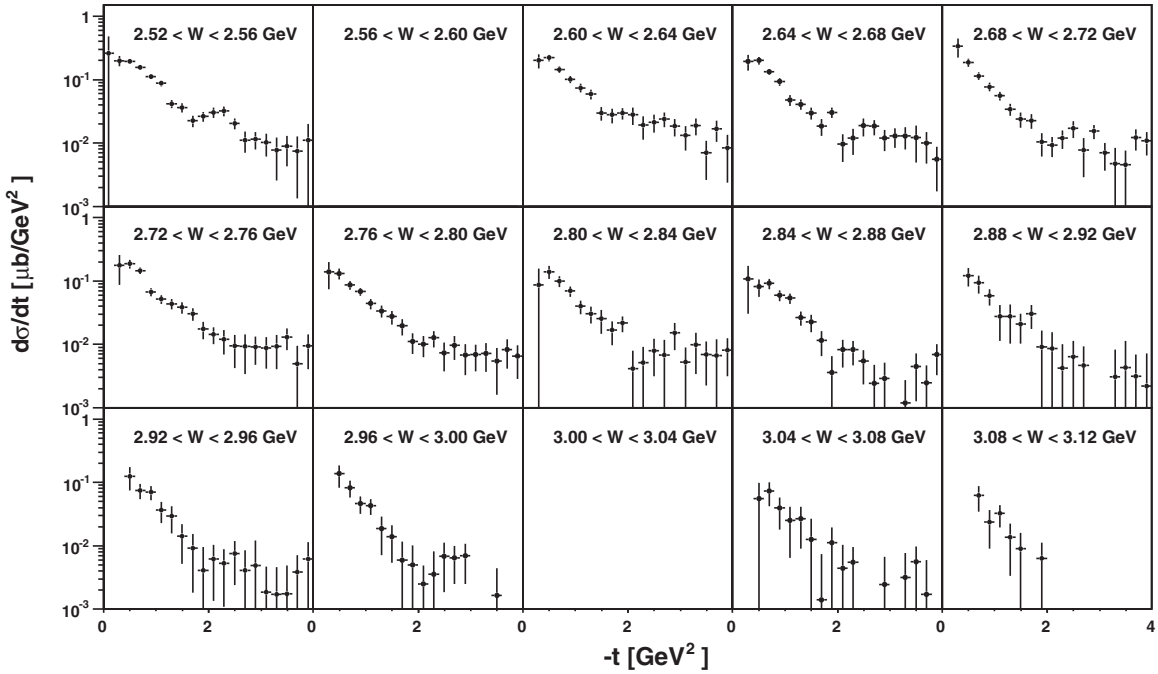

FIG. 20. The differential cross sections $d\sigma/dt$ in 40-MeV-wide center-of-mass bins for $W \in [2.52, 3.12]$ GeV and for the full range $-t \in [0, 4]$ GeV^2. The new CLAS data are shown as the black solid circles (•) and the uncertainties associated with each point are comprised of the statistical uncertainty and contributions from the Q-value correlation uncertainty added in quadrature.

CLAS-g11a data remains very good. Above $W = 2.72$ GeV ($E_\gamma \approx 3.5$ GeV), the presented data are first measurements. CLAS-g12 data are not available for the energy bin $2.56 < W < 2.60$ GeV, caused by an established tagger inefficiency in the detectors of the tagger focal plane in this region, and for the energy bin $3.00 < W < 3.04$ GeV because the total number of events in this bin was smaller than $N_c = 500$ (see Sec. IV D) and the background subtraction (using the Q-factor method) could not be performed. Figure 17 is similar to Fig. 16 but for the same W range of [2.36, 3.12] GeV, only shows the forward direction $0.5 < \cos\theta^{\eta}_{\text{c.m.}} < 1.0$ using an angle bin size of 0.05, which is a factor of two smaller than the binning used for the data shown in the previous figures. The reason for changing the binning in this representation of the data is to study more closely the t-channel production of η mesons beyond the baryon resonance regime and to compare the measured angular distributions with the model described in Ref. [3].

B. Differential cross sections $d\sigma/dt$

In an effort to study η photoproduction beyond the baryon resonance regime, the differential cross sections have been extracted also in a (W, $-t$) representation. This approach facilitates the comparison of the data with Regge models that aim at describing the reaction in terms of the t-channel exchange of massive quasi-particles. These new CLAS results are particularly important since they provide the missing data link in the energy range $E_\gamma \in [3.5, 4.5]$ GeV between the baryon resonance and the Regge-dominated regime.

Figure 18 shows the differential cross sections $d\sigma/dt$ for the energy range $W \in [2.52, 3.12]$ GeV corresponding to incident photon energies $E_\gamma \in [2.91, 4.72]$ GeV using 0.2-GeV^2-wide $-t$ bins for $0 < -t < 2$ GeV^2. Also shown in the figure are older data from NINA at the Daresbury Laboratory [35] for the energy bin $2.52 < W < 2.56$ GeV as well as data from DESY [36], the Cambridge Electron Accelerator at MIT [38], and Cornell [39], which are only available at $W = 2.9$ GeV. For the higher W bin, the comparison between the data from the 1960s and 1970s, and the CLAS data is also presented in Fig. 19 using a linear scale. The MIT data are consistent with the new CLAS results, whereas all other data are found to be significantly higher. The older data from DESY and Cornell were used to constrain the model developed by the Joint Physics Analysis Center (JPAC) [3] for $-t < 1.0$ GeV^2 at these fairly low energies in the Regge regime. This model is shown as a red long-dashed curve. While the Regge model of Ref. [3] describes the DESY and Cornell low-t data fairly well, the prediction clearly overestimates the experimental data points for $-t > 1.0$ GeV^2. The observed discrepancy between the older data (from DESY and Cornell) and the new CLAS data is indicative of the scale discrepancy between these new data and the JPAC curve.

The full set of new data points is shown in Fig. 20 for the entire analyzed $-t$ range, $0 < -t < 4$ GeV^2, on a logarithmic scale. The almost linear fall-off of the differential cross sections in the low $-t$ region is expected and can clearly be observed.

C. Comparison with previous CLAS data

Figure 21 shows a comparison of the new CLAS data with the previously published CLAS data on η photoproduction

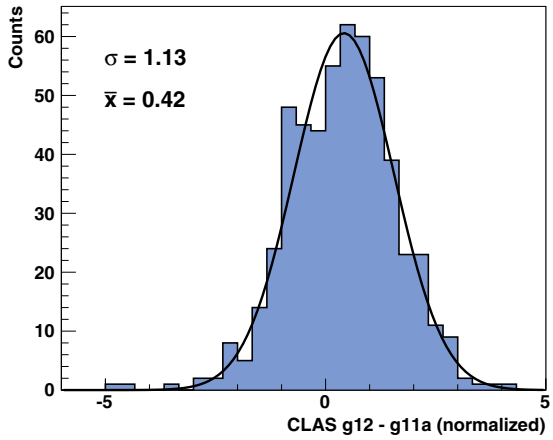

FIG. 21. Comparison between the new and the published [30] CLAS data in form of a difference distribution normalized to their uncertainties. See text for more details.

[30] in the form of a normalized difference distribution:

$$\frac{\left(\frac{d\sigma}{d\Omega}\right)_{\mathrm{g12}} - \left(\frac{d\sigma}{d\Omega}\right)_{\mathrm{g11a}}}{\sqrt{(\Delta\sigma)^2_{\mathrm{g12}} + (\Delta\sigma)^2_{\mathrm{g11a}}}}, \tag{17}$$

where the uncertainties in the denominator are comprised only of statistical and Q-value correlation uncertainties.

With the exception of a small structure around -1.0 due to a possible poorly understood acceptance effect in either experiment, the distribution is symmetric and Gaussian indicating that any discrepancies in the shape of the differential cross sections are mostly statistical in nature. The Gaussian width of $\sigma = 1.13$ suggests that the uncertainties in the denominator of Eq. (17) are slightly underestimated.

As a matter of fact, no additional uncertainties are included beyond those listed in Table II to guarantee consistency between the two data sets. However, the difference distribution is slightly shifted toward positive values. Figure 22 shows the unweighted ratio distribution of the same two data sets.

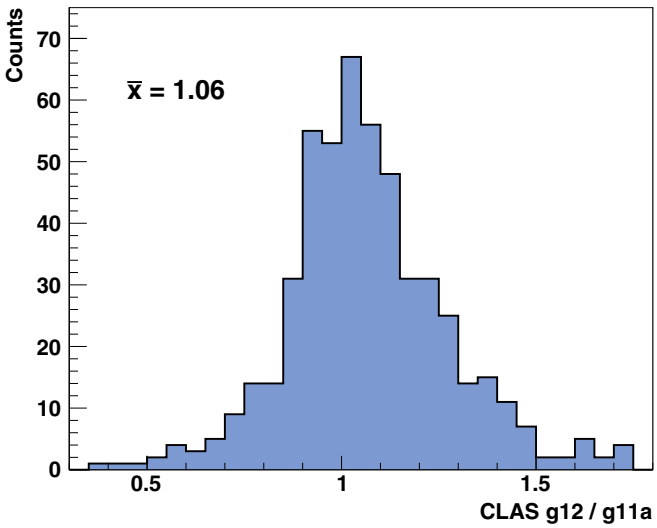

FIG. 22. Unweighted ratio distribution of the new and the published [30] CLAS data.

This distribution is also fairly symmetric with a mean value of 1.06, which indicates that an overall increase of about 6% is observed in the new data. The electron rates detected by the tagger and used to compute the number of photons incident on the target are integrated over the live time of the experiment. In the previous CLAS measurement [30], the clock-based live time calculation was checked by using the counts of a Faraday cup located downstream of CLAS. Despite high statistical uncertainties in these secondary measurements, a current-dependent live time was observed and at maximum electron beam current, the dead time was determined to be about a factor of two higher than the one given by the clock-based measurement used for the flux normalization. The corresponding correction resulted in the largest single-source contribution to the overall systematic uncertainty. Such a current-dependent live time was not observed for the CLAS-g12 data. The reason for this effect in the previous CLAS experiment remains poorly understood. However, the observed overall scale discrepancy between the two CLAS measurements of the $\gamma p \to p\eta$ cross sections is well within the reported uncertainties for these two experiments.

VII. PHYSICS DISCUSSION

Various theoretical and phenomenological approaches have been applied and studied to describe η photoproduction on the nucleon, in particular, to understand nucleon resonance contributions to this reaction, e.g., effective field theory [69], dispersion theoretical calculations [70], and Regge models [71,72].

A special group of models are isobar models, e.g., Refs. [73–75], which treat nucleon resonances in terms of s-channel Breit-Wigner parametrizations using energy-dependent widths due to their couplings with other decay channels. The nonresonant background amplitude is typically written as a sum of Born terms and t-channel meson-exchange contributions. In η photoproduction, Born terms are usually suppressed because their coupling constants are fairly small. In such isobar models, the double-counting of terms due to the quark-hadron duality is often concerning since the sum of an infinite series of s-channel resonances is equivalent to an infinite sum of t-channel meson-exchange amplitudes. In the η-MAID 2018 isobar model described in Ref. [4], the double-counting is removed by introducing a damping factor to the Regge amplitudes. Moreover, despite the minor role of Born terms, their couplings are determined from fitting experimental data.

The latest η-MAID 2018 solution is shown as a blue solid curve in Figs. 11–19. The experimental data are described very well over the entire energy range. All known N^* states listed in the RPP [22] were used to describe the resonance regime from the $\gamma p \to p\eta$ threshold up to $W < 2.5$ GeV. For a given partial wave α, the set of N_α nucleon resonances were added as generalized Breit-Wigner functions with a unitary phase ϕ for each resonance [4]. For the higher-energy regime, Regge phenomenology was applied and in an effort to provide a continuous description of η photoproduction from threshold to about $W \approx 5$ GeV, the damping fator was introduced, which goes to zero at the η production

threshold and approaches unity above $W = 2.5\,\text{GeV}$, where Regge description fully sets in Ref. [4]. Only two resonances were found to be insignificant in their contribution to $\gamma p \to p\eta$: The $N(2040)\,3/2^+$ resonance, a one-star state observed by BES II in J/ψ decays to $N\bar{N}\pi$ [76,77], and the $N(2220)\,9/2^+$ resonance. In their description, the reaction is dominated by the $1/2^-$ partial wave that is associated with contributions from the $N(1535)\,1/2^-$, $N(1650)\,1/2^-$, and $N(1895)\,1/2^-$ states. In the fourth resonance region, the most significant contributions beyond the $1/2^-$ partial wave come from the $N(1875)\,3/2^-$, $N(1900)\,3/2^+$, and the $N(1860)\,5/2^+$ nucleon resonances.

The multichannel Bonn-Gatchina (BnGa) partial wave analysis (PWA) uses a large experimental database, which includes data on pion- and photo-induced meson-production reactions, with up to two pseudoscalar mesons in the final state [78]. The approach is based on a fully relativistically invariant operator expansion method and combines the analysis of different reactions imposing directly analyticity and unitarity constraints [79]. Figures 11–15 show the BnGa solution BnGa 2019 as a purple curve; more details are discussed in Ref. [79]. Overall, the BnGa curve describes the experimental data very well. Deviations from the η-MAID 2018 solution can be observed, mostly in the forward direction above $W \approx 2\,\text{GeV}$. The difference between the two curves can be traced back to very similar discrepancies between the CLAS and CBELSA/TAPS data sets, which received different weights in the interpretation of the data. The $1/2^-$ partial wave also dominates the BnGa description of the $\gamma p \to p\eta$ reaction. However, in the fourth resonance region, the $N(1900)\,3/2^+$ resonance plays a significantly more important role than in η-MAID 2018, whereas contributions from the other two states found significant in η-MAID, $N(1875)\,3/2^-$ and $N(1860)\,5/2^+$, are practically negligible [80]. The identification of significant contributions from different nucleon resonances in η photoproduction is not surprising since the polarization observables are still scarce.

The high-energy regime above $E_\gamma = 4\,\text{GeV}$ is studied in terms of the Regge amplitudes discussed in Ref. [3]. While each Regge exchange has a known energy dependence, the t behavior is *a priori* unknown. In the approach of the Joint Physics Analysis Center (JPAC) [3], information from the resonance region is used through dispersion relations and finite-energy sum rules (FESR) to extract the t-dependence of the differential cross sections at high energies. Specifically, the η-MAID 2001 model [73] was used for the low-energy parametrizations. Data from DESY [36] and Cornell [39] for $0 < -t < 1\ \text{GeV}^2$ were used to constrain the JPAC model. The available data sets and the model are shown in Fig. 19 for $E_\gamma \approx 4.0\,\text{GeV}$. The red JPAC curve describes the DESY and the Cornell data well but is observed to be systematically off in its description of the new CLAS data and the data from MIT [38]. This scaling problem is also observed in Fig. 18.

For the Regge exchanges in the JPAC approach, two high-energy models have been developed. In the first more conservative approach, shown in Figs. 17–19, only t-channel exchanges associated with the known ($J^{PC} = 1^{--}$) vector- (ω, ρ) and ($J^{PC} = 1^{+-}$) axial-vector (h_1, b_1) meson resonances are considered, whereas the second model includes exchanges that correspond to, as yet, unobserved mesons. The latter approach explores the possible impact of a 2^{--} exchange that would result in increased cross sections and in a beam asymmetry smaller than one. The conservative JPAC predictions are observed to systematically overestimate the new CLAS data and the inclusion of a 2^{--} exchange would only increase this discrepancy. The preliminary conclusion is that these new data and more importantly, recent results on the beam asymmetry in η photoproduction at high energies reported by the GlueX Collaboration [24,81] are in clear contradiction with these predictions. The 2^{--} exchange has also not been considered in the η-MAID 2018 model. The C-parity conservation prohibits exchanges of scalar and pseudoscalar mesons.

In conclusion, these experimental data confirm the expectation that the $\gamma p \to p\eta$ reaction proceeds primarily through ρ and ω vector-meson 1^{--} exchange. Other η data also confirm the predicted rapid decline of the cross sections in the very forward direction of the η meson in the center-of-mass frame, which corresponds to the differential cross sections at very small values of $-t$. This behavior is clearly visible in the model descriptions shown in Figs. 17–19. For $\cos\theta_{\text{c.m.}} = 1$ or $t' = t - t_{\text{min}} = 0\ \text{GeV}^2$, conservation of angular momentum requires conservation of helicities:

$$\lambda_\gamma - \lambda_{\text{proton}} = \lambda_\eta - \lambda_{\text{proton}'}, \tag{18}$$

where the right-hand side denotes the helicity of the recoiling proton with $\lambda_\eta = 0$. In Regge models, this imposes an even stronger constraint since conservation of angular momentum is required at the top (γ-η) vertex and at the bottom (N-N) vertex in the right diagram of Fig. 1. Since the helicity of a real photon, $\lambda = \pm 1$, cannot turn into $\lambda = 0$ for the η meson, the amplitude needs to vanish and the cross section decreases to *zero*. In Regge pole theory, this behavior is thus built into the top vertex by factorization [1]. In contrast, using virtual photons, the cross section in the very forward direction proceeds primarily via the photon's longitudinal component.

VIII. SUMMARY AND OUTLOOK

Photoproduction cross sections have been presented for the reaction $\gamma p \to p\eta$ using tagged photons and the CLAS spectrometer at Jefferson Laboratory. The results are shown for incident photon energies between about 1.2 and 4.7 GeV. These new η photoproduction data are consistent with earlier CLAS results but extend the energy range beyond the nucleon resonance regime. Cross sections $d\sigma/dt$ are also presented for $W > 2.52\,\text{GeV}$ and studied in terms of the dominant Regge exchange amplitudes. While axial vector exchanges are negligible, the data confirm the expected dominance of vector-meson exchanges. Calculations using finite-energy sum rules (FESR) indicate that the 2^{--} exchange could be relevant but predictions are inconsistent with the differential cross section data presented here and with beam-asymmetry results recently reported by the GlueX Collaboration. In light of these new CLAS-g12 data and the new η-MAID 2018 model, it would certainly be interesting to revisit the JPAC approach. Upcoming data from the GlueX Collaboration will extend the differential cross section measurements to

$W \approx 4.2$ GeV and further prepare the foundation for a global analysis of low- and high-energy data of related reactions within the framework of FESR.

In the baryon resonance regime, a comparison of the differential cross sections $d\sigma/d\Omega$ with predictions of the isobar model η-MAID 2018 and the BnGa coupled-channel analysis confirms the dominance of the $1/2^-$ partial wave close to the reaction threshold. The unambiguous identification of resonance contributions in the fourth resonance region is still challenging owing to the lack of polarization observables around $W \approx 2$ GeV.

ACKNOWLEDGMENTS

The authors thank the technical staff at Jefferson Laboratory and at all the participating institutions for their invaluable contributions to the success of the experiment. This research is based on work supported by the US Department of Energy, Office of Science, Office of Nuclear Physics, under Contract No. DE-AC05-06OR23177. The group at Florida State University acknowledges additional support from the US Department of Energy, Office of Science, Office of Nuclear Physics, under Contract No. DE-FG02-92ER40735. This work was also supported by the US National Science Foundation, the State Committee of Science of Republic of Armenia, the Chilean Comisión Nacional de Investigación Científica y Tecnológica (CONICYT), the Italian Istituto Nazionale di Fisica Nucleare, the French Centre National de la Recherche Scientifique, the French Commissariat a l'Energie Atomique, the Scottish Universities Physics Alliance (SUPA), the United Kingdom's Science and Technology Facilities Council, and the National Research Foundation of Korea.

[1] A. C. Irving and R. P. Worden, Phys. Rep. **34**, 117 (1977).
[2] V. Mathieu, J. Nys, C. Fernández-Ramírez, A. N. Hiller Blin, A. Jackura, A. Pilloni, A. P. Szczepaniak, and G. Fox (JPAC Collaboration), Phys. Rev. D **98**, 014041 (2018).
[3] J. Nys *et al.* (JPAC Collaboration), Phys. Rev. D **95**, 034014 (2017).
[4] L. Tiator *et al.*, Eur. Phys. J. A **54**, 210 (2018).
[5] V. Mathieu, G. Fox, and A. P. Szczepaniak, Phys. Rev. D **92**, 074013 (2015).
[6] V. Mathieu, I. V. Danilkin, C. Fernandez-Ramirez, M. R. Pennington, D. Schott, A. P. Szczepaniak, and G. Fox, Phys. Rev. D **92**, 074004 (2015).
[7] B. A. Mecking *et al.*, Nucl. Instrum. Methods Phys. Res., Sect. A **503**, 513 (2003).
[8] W. Hillert, Eur. Phys. J. A **28**, 139 (2006).
[9] B. A. Mecking, Eur. Phys. J. A **28**, 209 (2006).
[10] O. Bartalini *et al.* (GRAAL Collaboration), Eur. Phys. J. A **26**, 399 (2005).
[11] N. Muramatsu *et al.* (LEPS Collaboration), Nucl. Instrum. Methods Phys. Res., Sect. A **737**, 184 (2014).
[12] B. Krusche *et al.*, Phys. Rev. Lett. **74**, 3736 (1995).
[13] B. Krusche *et al.*, Phys. Lett. B **397**, 171 (1997).
[14] J. Ajaka *et al.*, Phys. Rev. Lett. **81**, 1797 (1998).
[15] D. Elsner *et al.* (CBELSA and TAPS Collaborations), Eur. Phys. J. A **33**, 147 (2007).
[16] O. Bartalini *et al.* (GRAAL Collaboration), Eur. Phys. J. A **33**, 169 (2007).
[17] P. Collins *et al.* (CLAS Collaboration), Phys. Lett. B **771**, 213 (2017).
[18] C. S. Akondi *et al.* (A2 at MAMI Collaboration), Phys. Rev. Lett. **113**, 102001 (2014).
[19] I. Senderovich *et al.* (CLAS Collaboration), Phys. Lett. B **755**, 64 (2016).
[20] L. Witthauer *et al.* (A2 Collaboration), Phys. Rev. C **95**, 055201 (2017).
[21] J. Müller *et al.* (CBELSA/TAPS Collaboration), Phys. Lett. B **803**, 135323 (2020).
[22] M. Tanabashi *et al.* (Particle Data Group), Phys. Rev. D **98**, 030001 (2018).
[23] B. Krusche and C. Wilkin, Prog. Part. Nucl. Phys. **80**, 43 (2014).
[24] H. Al Ghoul *et al.* (GlueX Collaboration), Phys. Rev. C **95**, 042201 (2017).
[25] S. Adhikari *et al.* (GlueX Collaboration), Nucl. Instrum. Meth. A **987**, 164807 (2021).
[26] F. Renard *et al.* (GRAAL Collaboration), Phys. Lett. B **528**, 215 (2002).
[27] M. Sumihama *et al.* (LEPS Collaboration), Phys. Rev. C **80**, 052201 (2009).
[28] V. Crede *et al.* (CB-ELSA Collaboration), Phys. Rev. Lett. **94**, 012004 (2005).
[29] O. Bartholomy *et al.* (CB-ELSA Collaboration), Eur. Phys. J. A **33**, 133 (2007).
[30] M. Williams *et al.* (CLAS Collaboration), Phys. Rev. C **80**, 045213 (2009).
[31] V. Crede *et al.* (CBELSA/TAPS Collaboration), Phys. Rev. C **80**, 055202 (2009).
[32] E. F. McNicoll *et al.* (Crystal Ball at MAMI Collaboration), Phys. Rev. C **82**, 035208 (2010); **84**, 029901(E) (2011).
[33] V. L. Kashevarov *et al.* (A2 Collaboration), Phys. Rev. Lett. **118**, 212001 (2017).
[34] D. G. Ireland, E. Pasyuk, and I. Strakovsky, Prog. Part. Nucl. Phys. **111**, 103752 (2020).
[35] P. J. Bussey *et al.*, Phys. Lett. B **61**, 479 (1976).
[36] W. Braunschweig *et al.*, Phys. Lett. B **33**, 236 (1970).
[37] V. B. Elings *et al.*, Phys. Rev. **156**, 1433 (1967).
[38] D. Bellenger, S. Deutsch, D. Luckey, L. S. Osborne, and R. Schwitters, Phys. Rev. Lett. **21**, 1205 (1968).
[39] J. Dewire, B. Gittelman, R. Loe, E. C. Loh, D. J. Ritchie, and R. A. Lewis, Phys. Lett. B **37**, 326 (1971).
[40] R. L. Anderson *et al.*, Phys. Rev. Lett. **21**, 384 (1968).
[41] A. Boyarski *et al.*, Phys. Rev. Lett. **20**, 300 (1968).
[42] A. Boyarski *et al.*, Phys. Rev. Lett. **22**, 1131 (1969).
[43] R. L. Anderson, Nucl. Instrum. Methods **65**, 195 (1968).
[44] E. Aker *et al.* (Crystal Barrel Collaboration), Nucl. Instrum. Methods Phys. Res., Sect. A **321**, 69 (1992).
[45] D. Werthmüller *et al.* (A2 Collaboration), Phys. Rev. C **90**, 015205 (2014).
[46] I. Jaegle *et al.* (CBELSA/TAPS Collaboration), Eur. Phys. J. A **47**, 89 (2011).
[47] L. Witthauer *et al.* (CBELSA/TAPS Collaboration), Eur. Phys. J. A **53**, 58 (2017).

[48] M. Dugger *et al.* (CLAS Collaboration), Phys. Rev. Lett. **89**, 222002 (2002); **89**, 249904(E) (2002).
[49] R. A. Arndt *et al.*, http://gwdac.phys.gwu.edu.
[50] V. Crede and W. Roberts, Rep. Prog. Phys. **76**, 076301 (2013).
[51] S. Chandavar *et al.* (CLAS Collaboration), Phys. Rev. C **97**, 025203 (2018).
[52] M. C. Kunkel *et al.* (CLAS Collaboration), Phys. Rev. C **98**, 015207 (2018).
[53] J. Bono *et al.* (CLAS Collaboration), Phys. Lett. B **783**, 280 (2018).
[54] J. T. Goetz *et al.* (CLAS Collaboration), Phys. Rev. C **98**, 062201 (2018).
[55] M. D. Mestayer *et al.*, Nucl. Instrum. Methods Phys. Res., Sect. A **449**, 81 (2000).
[56] E. S. Smith *et al.*, Nucl. Instrum. Methods Phys. Res., Sect. A **432**, 265 (1999).
[57] Y. G. Sharabian *et al.*, Nucl. Instrum. Methods Phys. Res., Sect. A **556**, 246 (2006).
[58] D. I. Sober *et al.*, Nucl. Instrum. Methods Phys. Res., Sect. A **440**, 263 (2000).
[59] CLAS-g12 Run Group, CLAS-NOTE 2017-002 (2017), https://misportal.jlab.org/ul/Physics/Hall-B/clas/viewFile.cfm/2017-002?documentId=756.
[60] E. Pasyuk, Jefferson Laboratory Report No. CLAS-NOTE 2007-016 (2007), https://misportal.jlab.org/ul/physics/Hall-B/clas/viewFile.cfm/2007-016.pdf?documentId=423.
[61] S. Brandt, *Data Analysis* (Springer-Verlag, New York, 1999).
[62] R. Brun, F. Bruyant, F. Carminati, S. Giani, M. Maire, A. McPherson, G. Patrick, and L. Urban, doi:10.17181/CERN.MUHF.DMJ1.
[63] M. Williams, M. Bellis, and C. A. Meyer, J. Instrum. **4**, P10003 (2009).
[64] M. Williams *et al.* (CLAS Collaboration), Phys. Rev. C **80**, 065208 (2009).
[65] P. Weidenauer *et al.* (ASTERIX Collaboration), Z. Phys. C **59**, 387 (1993).
[66] T. Hu *et al.* (CLAS Collaboration) (unpublished).
[67] J. Ball and E. Pasyuk, CLAS Note 2005-002 (2005), https://misportal.jlab.org/ul/Physics/Hall-B/clas/viewFile.cfm/2005-002.pdf?documentId=24.
[68] A. Wilson *et al.* (CBELSA/TAPS Collaboration), Phys. Lett. B **749**, 407 (2015).
[69] D. Ruić, M. Mai, and U.-G. Meißner, Phys. Lett. B **704**, 659 (2011).
[70] I. G. Aznauryan, Phys. Rev. C **68**, 065204 (2003).
[71] A. Sibirtsev, J. Haidenbauer, S. Krewald, and U.-G. Meißner, Eur. Phys. J. A **46**, 359 (2010).
[72] V. L. Kashevarov, M. Ostrick, and L. Tiator, Phys. Rev. C **96**, 035207 (2017).
[73] W. T. Chiang, S. N. Yang, L. Tiator, and D. Drechsel, Nucl. Phys. A **700**, 429 (2002).
[74] W. T. Chiang, S. N. Yang, L. Tiator, M. Vanderhaeghen, and D. Drechsel, Phys. Rev. C **68**, 045202 (2003).
[75] V. A. Tryasuchev, Eur. Phys. J. A **22**, 97 (2004).
[76] M. Ablikim *et al.* (BES Collaboration), Phys. Rev. Lett. **97**, 062001 (2006).
[77] M. Ablikim *et al.* (BES Collaboration), Phys. Rev. D **80**, 052004 (2009).
[78] http://pwa.hiskp.uni-bonn.de/baryon_x.htm.
[79] A. V. Anisovich *et al.*, Eur. Phys. J. A **52**, 284 (2016).
[80] A. V. Anisovich *et al.*, Phys. Rev. C **96**, 055202 (2017).
[81] S. Adhikari *et al.* (GlueX Collaboration), Phys. Rev. C **100**, 052201 (2019).